https://doi.org/10.1146/annurev-earth-031621-063756

Ductile Deformation of the Lithospheric Mantle

Jessica M. Warren[1] and Lars N. Hansen[2]

[1]Department of Earth Sciences, University of Delaware, Newark, DE, USA; warrenj@udel.edu; https://orcid.org/0000-0002-4046-4200

[2]Department of Earth and Environmental Sciences, University of Minnesota, Minneapolis, MN, USA; lnhansen@umn.edu; https://orcid.org/0000-0001-6212-1842

Shortened running title (40 characters max): Ductile Deformation of the Lithosphere

Keywords

1. deformation mechanisms
2. ductile flow
3. lithosphere
4. mantle
5. olivine
6. plasticity

Length: Abstract = 151 words; Main text = 7697 words; Sidebars = 1093 words; References = 165 citations; Tables=1; Figures=8

Submitted to Annual Reviews of Earth and Planetary Sciences on 7/17/2022

Revisions submitted to Annual Reviews of Earth and Planetary Sciences on 10/19/2022

Abstract

The strength of lithospheric plates is a central component of plate tectonics, governed by brittle processes in the shallow portion and ductile behavior in the deeper portion. We review experimental constraints on ductile deformation of olivine, the main mineral in the upper mantle and thus the lithosphere. Olivine deforms by four major mechanisms: low-temperature plasticity, dislocation creep, dislocation-accommodated grain-boundary sliding (GBS), and diffusion-accommodated grain-boundary sliding (diffusion creep). Deformation in most of the lithosphere is dominated by GBS, except in shear zones—in which diffusion creep dominates—and in the brittle-ductile transition—in which low-temperature plasticity may dominate. We find that observations from naturally deformed rocks are consistent with extrapolation of the experimentally constrained olivine flow laws to geological conditions, but that geophysical observations predict a weaker lithosphere. The causes of this discrepancy are unresolved, but likely reside in the uncertainty surrounding processes in the brittle-ductile transition, where the lithosphere is strongest.

1. Introduction

The strength of the lithosphere is a central component of plate tectonics, controlling processes such as plate flexure, post-seismic rebound, formation of plate boundaries, and differences in the behavior of continental versus oceanic plates (Figure 1). Deformation in the upper part of plates is governed by brittle failure and friction (e.g., Brace & Byerlee 1966, Dieterich 2007), followed by a transition to ductile behavior at depths of ~5–50 km, depending on thermal structure and plate composition. Both laboratory data (e.g., Kohlstedt et al. 1995) and geophysical observations (e.g., England & Molnar 2015) suggest that the strongest part of the lithosphere is usually at the brittle-ductile transition in the mantle. In oceanic plates, the crust is generally too thin (~6 km) and cold for ductile deformation, with the brittle-ductile transition occurring in the shallow upper mantle. In continental lithosphere, the depth of the brittle-ductile transition depends on the composition, water content, and thermal structure of the crust. In some places, a weak ductile lower crust overlies brittlely deforming mantle, while in other places the lower crust is stronger than the mantle (e.g., Bürgmann & Dresen 2008). In both oceanic and continental plates, the transition to fully ductile behavior occurs in the mantle at temperatures of 600–700°C (e.g., Abercrombie & Ekström 2001, Boettcher et al. 2007), which corresponds to a depth of ~5 km in the youngest oceanic crust and becomes progressively deeper elsewhere, where cooling has thickened the upper, brittle layer. As the average thickness of oceanic plates is ~120 km and of continental plates is <250 km (e.g., Fischer et al. 2020, Richards et al. 2020), the ductile behavior of the lithospheric mantle dominates the integrated strength of plates (e.g., England & Molnar 2015).

Constraints on ductile deformation of the lithosphere come from laboratory experiments, natural samples, micromechanical models, and geophysical observations (e.g., Kohlstedt et al. 1995). Lab

experiments provide quantitative constraints on the constitutive equations that describe the deformation of mineral aggregates (e.g., Griggs 1936, Paterson 1970). These data are typically collected on monophase aggregates at fast strain rates (~10^{-4}–10^{-6} s^{-1}) compared to tectonic strain rates (10^{-12}–10^{-16} s^{-1}), with extrapolations necessary of one or more other parameters (e.g., stress, temperature, and/or grain size). Field and microstructural studies of naturally deformed rocks are used to constrain conditions of deformation and validate the extrapolation of experimental data. Micromechanical models provide further insight into deformation processes at atomic (for a review, see Piazolo et al. 2019) to plate length-scales (e.g., Breithaupt et al. 2020, Gouriet et al. 2019). Ultimately, the goal of experimental, field, and modeling studies is to develop flow laws that can be applied to a broad range of geophysical problems (e.g., Billen 2008, Whitehouse 2018) and to test the robustness of interpretations of geophysical observations (e.g., England & Molnar 2015, Watts et al. 2013).

This paper reviews the current state of knowledge of steady-state ductile deformation of the lithospheric mantle. Transient ductile creep is described by Faul & Jackson (2015), Hansen et al. (2021) and Karato (2021). Ductile deformation of the crust is evaluated by Bürgmann & Dresen (2008), while brittle processes are reviewed by Brantut et al. (2013) and Hoek & Martin (2014) and frictional behavior by Marone (1998). Here, we first provide an update to the compilation of laboratory-derived flow laws of Hirth & Kohlstedt (2003). We then describe the use of natural samples to validate experimental datasets and compare flow law predictions for lithospheric strength to geophysical constraints, before discussing future directions.

2. Laboratory constraints on mantle rheology, along with revisions and caveats

As olivine is the most abundant mineral in the upper mantle, the majority of experimental constraints for mantle rheology are provided by experiments on olivine aggregates and single crystals (e.g., Carter 1976, Hirth & Kohlstedt 2003, Karato & Wu 1993). In this section, we describe updates and revisions to flow laws since the compilation by Hirth & Kohlstedt (2003), which provided a detailed analysis of experimental constraints on the ductile deformation of olivine.

Steady-state creep in minerals is accommodated by multiple deformation mechanisms that operate simultaneously. These mechanisms fundamentally involve an applied stress that produces strain through the movement of crystal defects (Figure 2), with the kinetics of this movement setting the overall strain rate (for reviews, see Demouchy 2021, Kohlstedt & Hansen 2015). For olivine, the major processes observed to produce deformation are dislocation glide (e.g., Durham et al. 1977, Idrissi et al. 2016), mass diffusion (Hirth & Kohlstedt 1995a, Yabe et al. 2020), and grain-boundary sliding (Bollinger et al. 2019, Maruyama & Hiraga 2017), as illustrated in Figure 2. Various combinations of these processes set the kinetics of the four main deformation mechanisms that have been identified in olivine: low-temperature plasticity, dislocation creep, dislocation-accommodated grain-boundary sliding (or more simply GBS), and diffusion-accommodated grain-boundary sliding (more commonly referred to as diffusion creep). Each mechanism has a regime where it dominates by producing strain at rates that are orders of magnitude faster than the other mechanisms. The boundaries between regimes are defined by the conditions (pressure, temperature, grain size, stress) at which two mechanisms produce strain at equivalent rates.

Some confusion stems from the standard nomenclature for deformation mechanisms as the terminology is often misleading. Low-temperature plasticity is not restricted to low temperatures, since dislocation glide and dislocation interactions (Figure 2) can easily dominate the mechanical behavior at elevated temperatures if the applied stress is high enough (e.g., Faul et al. 2011). This mechanism is also inherently a part of dislocation creep, since in both cases the rate of dislocation glide sets the overall strain rate. The key distinction is that, in the latter case, the dislocation climb velocity begins to influence the dislocation glide velocity (e.g., Hansen et al. 2021). In addition, grain-boundary sliding (Figure 2) is often used to refer solely to dislocation accommodation, even though diffusion creep also involves sliding on grain boundaries (Raj & Ashby 1971). Further adding to potential confusion, sliding actually appears to contribute very little to the overall strain (most of the strain being intragranular) in the case of dislocation accommodation, whereas sliding contributes most of the strain in diffusion creep (Bollinger et al. 2019, Langdon 2006, Maruyama & Hiraga 2017). Despite such caveats to the common nomenclature, we maintain the standard terminology here so as to prevent further confusion by introducing new jargon.

Theoretical and experimental observations of steady-state creep in rocks, metals, and ceramics (e.g., Carter 1976, Dorn 1955, Weertman & Weertman 1975) indicate that most deformation mechanisms (with the exception of low-temperature plasticity) can be described by the semi-empirical constitutive equation

$$\dot{\varepsilon}_i = A_i \frac{\sigma^{n_i}}{d^{p_i}} c_{\mathrm{OH}}^{r_i} \exp\left(\alpha_i \phi\right) \exp\left(\frac{-\left(E_i^* + PV_i^*\right)}{\mathrm{R}T}\right). \quad (1)$$

The parameter $\dot{\varepsilon}$ is the steady-state strain rate, A is a pre-exponential factor, σ is differential stress, n is the stress exponent, d is grain size, m is the grain-size exponent, c_{OH} is water concentration, r is the water-concentration exponent, α describes the melt-fraction dependence, ϕ is the melt

fraction, E^* is activation energy, P is pressure, V^* is activation volume, R is the ideal gas constant, and T is absolute temperature. The subscript i indicates the ith deformation mechanism.

Equation 1 is appropriate for steady-state creep if differential stress and strain rate are constant. Sidebars on the Pre-Exponential Factor, Water Fugacity and Concentration, and Activation Volume provide clarifications for some of the terms in this equation. The effects of chemical parameters such as oxygen fugacity, silica activity, and iron content are discussed in the sidebar titled Chemical Environment. The influence of melt on deformation is reviewed by Katz et al. (2022).

The total strain rate for an olivine aggregate is described by a combination of the individual flow laws

$$\dot{\varepsilon}_{\text{total}} = \sum_i \dot{\varepsilon}_i = \dot{\varepsilon}_{\text{ltp}} + \dot{\varepsilon}_{\text{disc}} + \dot{\varepsilon}_{\text{gbs}} + \dot{\varepsilon}_{\text{diff}}, \tag{2}$$

where "total" indicates the total strain rate, "ltp" is low-temperature plasticity, "disc" is dislocation creep, "gbs" is grain-boundary sliding, and "diff" is diffusion creep. Table 1 presents an update to the compilation of flow law parameters presented by Hirth & Kohlstedt (2003), which we explore in the following sections.

2.1. Low-temperature plasticity

Flow laws for low-temperature plasticity are generally based on the kinetics of dislocation glide (see Chapters 3 and 4 in Kocks et al. 1975; Figure 2), which accounts for the difficulty in dislocations gliding past obstacles. The classic form (Chapter 2 in Frost & Ashby 1982) of this flow law is

$$\dot{\varepsilon}_{\mathrm{ltp}} = A_{\mathrm{ltp}} \exp\left\{-\frac{E^*_{\mathrm{ltp}}}{\mathrm{R}T}\left[1-\left(\frac{\sigma}{\Sigma}\right)^s\right]^q\right\}, \quad (3)$$

where Σ is the Peierls stress and s and q are material constants that describe the shape of the potential barrier the dislocations need to overcome. Sometimes this flow law is written with an additional σ^2 term outside of the exponential term to account for the influence of stress on the dislocation density.

Based on recent experiments, Hansen et al. (2019, 2021) provided an updated flow law built on the inference that long-range interactions among dislocations are the primary barrier to motion,

$$\dot{\varepsilon}_{\mathrm{ltp}} = A_{\mathrm{ltp}}\rho \sinh\left(-\frac{E^*_{\mathrm{ltp}}}{\mathrm{R}T}\right)\sinh\left(\frac{E^*_{\mathrm{ltp}}}{\mathrm{R}T}\frac{\sigma-\sigma_{\mathrm{b}}}{\Sigma}\right), \quad (4)$$

where ρ is the dislocation density and σ_{b} is the backstress (Table 1). This flow law makes the simplifying assumption that s and q in Equation 3 are unity. The sinh term results in a symmetric equation such that the flow law is applicable to positive and negative stresses and strain rates.

Both ρ and σ_{b} may evolve during deformation, which leads to changes in stress or strain rate as a function of strain. In most instances, an increase in σ_{b} is the prominent effect (Hansen et al. 2021), which leads to decreasing strain rates or increasing stresses as strain increases. To predict this strain hardening, σ_{b} must be tracked (Mecking & Kocks 1981), which has recently been described for olivine (Breithaupt et al. 2020, Hansen et al. 2019, 2021). For the purposes of this review, we focus on two end-member cases (Table 1): 1) the yield behavior at the onset of deformation prior to strain hardening and 2) the steady-state behavior at large strains. At yield, σ_{b} is taken to be negligible, though there must be some preexisting dislocations or else deformation cannot proceed at all. Thus, we use an initial dislocation density of 10^{10} m^{-2}, which is comparable to the dislocation density in pristine natural olivine (Toriumi & Karato 1978). For steady-state, σ_{b} is set to the

experimentally determined value of 1800 MPa, which Hansen et al. (2019) suggested relates to the maximum possible dislocation density. This backstress corresponds to a value of $\rho = 10^{14.8}$ m^{-2} for steady-state deformation according to the recent calibration for olivine (Thom et al. 2022). Due to the strong covariance between A_{ltp} and E_{ltp}* (see sidebar on the Pre-Exponential Factor), this flow law provides poor constraints on E_{ltp}* (Hansen et al. 2021). In Table 1, we provide the values for A_{ltp} and E_{ltp}* from Breithaupt et al. (2020) since they lead to a self-consistent prediction about the relationship between dislocation density and stress, as discussed in the next section.

The flow law for low-temperature plasticity is illustrated in Figure 3. Across a wide range of temperatures, low-temperature plasticity results in nearly rate-independent deformation at very high stresses and therefore sets the maximum strength of crystal-plastic deformation in olivine. Figure 3 also presents the model from Gouriet et al. (2019), which was derived from small-scale, discrete-dislocation-dynamics simulations. These simulations predict much lower stresses (at high strain rates) than observed in experiments and predicted by the flow laws in Table 1, which suggests that they do not capture the full magnitude of strain hardening exhibited by olivine.

The influence of grain size and water content are not included in the flow laws for low-temperature plasticity in Table 1. Grain sizes that are <10's μm lead to strengthening, which is critical to account for in comparisons among laboratory-based studies (Hansen et al. 2019, Kumamoto et al. 2017), but less relevant to fine-grained shear zones in the Earth deforming by diffusion creep (see section 3.2). Some data at the boundary between dislocation creep and low-temperature plasticity suggest that increasing the olivine water content leads to weakening (Katayama & Karato 2008), but recent experiments on olivine in the low-temperature plasticity regime suggest that water has no effect (Kumamoto et al. 2021).

2.2. Dislocation creep

Dislocation creep inherently involves similar processes as low-temperature plasticity since strain is still produced by dislocation glide (Figure 2). However, flow laws for dislocation creep are based on the kinetics of dislocation climb (Figure 2) since climb allows dislocations to be removed via annihilation (i.e., dislocation recovery), which counteracts the dislocation interactions that produce strain hardening. At steady state, dislocation creep is therefore controlled by dislocation climb and can be described with the power-law relationship presented in Equation 1 and illustrated in Figure 3.

Of the parameters in this flow law, the stress dependence of dislocation creep, n_{disc}, has been the focus of considerable discussion (e.g., Freed et al. 2012, Hirth & Kohlstedt 2015, Jain et al. 2019). Uncertainty in n_{disc} results in large uncertainty in mantle viscosity and in interpretation of the fundamental underlying processes. Statistical exploration of olivine experimental datasets highlights the nonlinear nature of parameter estimation (Jain et al. 2019), which is particularly acute due to the narrow range of conditions over which experiments can be conducted. Additional complexity occurs from the need to control extensive variables such as silica activity, water content, oxygen fugacity, and impurity concentration. Relatively minor differences among experiments can propagate to large uncertainties in deformation variables and purely numerical fits of datasets generally do not account for the linked physical constraints (e.g., Jain et al. 2019).

Given the limitations of experiments and statistical models for exploring the full range of parameter space, constraints on n_{disc} can instead be derived by combining laboratory data with analysis of the micromechanical processes accommodating creep. The preferred value for the stress exponent ($n_{disc} \approx 3.5$) in Table 1 is based on laboratory experiments evaluated against the

dislocation creep model for olivine (Hirth & Kohlstedt 2015). Microstructural observations of olivine suggest that dislocation creep is climb-limited (e.g., Durham et al. 1977). The climb velocity of dislocations is determined by the slowest diffusing component, which in olivine is controlled by the very slow diffusion of Si (e.g., Fei et al. 2012, 2013). However, implementation of this diffusivity in classic models of dislocation creep results in strain rate estimates that are 3 to 5 orders of magnitude smaller than observed in olivine deformation experiments (Hirth & Kohlstedt 2015). The diffusion of Si in wet olivine is also relatively slow and has been used to suggest that water does not influence creep rates (Fei et al. 2013) due to a similar underprediction of strain rates. The use of Si lattice diffusivities to constrain dislocation creep additionally leads to the prediction that the mantle does not undergo dislocation creep (Hirth & Kohlstedt 2015). However, observations of seismic anisotropy and peridotite microstructures suggest that dislocation creep dominates in the upper mantle (e.g., Karato et al. 2008, Mainprice & Silver 1993).

Hirth & Kohlstedt (2015) suggested that these issues can be reconciled if the dislocation climb velocity in olivine is instead limited by rapid Si pipe diffusion along dislocation cores. As the region within a few unit cells of a dislocation, dislocation cores have an especially large distortion of the crystal structure and provide a fast diffusion pathway. Considering that steady-state dislocation density is observed to scale with stress (Bai & Kohlstedt 1992, Karato & Jung 2003) and that the effective diffusivity of Si pipe diffusion depends on the dislocation density, Hirth & Kohlstedt (2015) derived a value of $n_{\mathrm{disc}} \approx 3.5$. In support of this assessment, Breithaupt et al. (2020) developed a microphysical model for olivine deformation that tracks the evolution of dislocation density, including the effects of pipe diffusion on dislocation recovery. Their model does not result in a flow law with a power-law form, but it does self-consistently predict the

observed relationship between dislocation density and stress and can be approximated by a power law with $n_{disc} \approx 3.5$ (Figure 3).

Dislocation creep is only predicted to be the dominant mechanism in the lithospheric mantle at moderate stresses combined with the largest grain sizes and highest temperatures (Figure 3c). The models from Gouriet et al. (2019) and Breithaupt et al. (2020) both predict an apparent n_{disc} close to 3.5 at these conditions. Due to their calibration involving dislocation density data as a function of stress, the model from Breithaupt et al. (2020) additionally predicts a transition to $n_{disc} \approx 5$ at higher stresses. This transition occurs due to the increasing influence of pipe diffusion at high dislocation densities and is followed by a transition to low-temperature plasticity at the highest stresses.

2.3. Dislocation-accommodated grain-boundary sliding

The third major regime for ductile deformation of olivine, GBS, is also referred to as dislocation-accommodated grain-boundary sliding (i.e., disGBS) or grain-size-sensitive dislocation creep. This terminology is used to distinguish it from diffusion creep, which is also a mechanism involving grain-boundary sliding, but for simplicity we use the abbreviation GBS in this review. In typical models of GBS, grain boundaries are relatively weak, allowing grains to slide past each other (Figure 2), but sliding is accompanied by deformation due to the motion of lattice dislocations, which sets the overall strain rate (e.g., Kassner 2015, Chapter 6).

Olivine was originally suggested to deform by GBS by Hirth & Kohlstedt (1995b) and a flow law was provided in Hirth & Kohlstedt (2003). More recently, this flow law has been revised based on

229 the experiments of Hansen et al. (2011). In the model proposed by Hirth & Kohlstedt (2003), GBS
230 was a serial combination of GBS and intracrystalline dislocation glide on the easiest slip system
231 in olivine. This formulation was motivated by the similarity of laboratory data for fine-grained
232 olivine to that of ice deforming by GBS (Goldsby & Kohlstedt 2001). The experiments by Hansen
233 et al. (2011) confirmed the occurrence of a regime for olivine in which strain rate exhibits a
234 nonlinear stress dependence ($n_{gbs} \approx 3$) and a finite grain-size sensitivity ($p_{gbs} \approx 1$), but Hansen et
235 al. (2011) argued that a regime limited by easy slip has not yet been documented in olivine, and
236 therefore we do not include a related flow law here.

237 The mild grain-size sensitivity of $p_{gbs} \approx 1$ results in grain-size sensitive deformation over a wide
238 range of grain sizes. This effect is illustrated in Figure 4, which compares data from experiments
239 to flow laws without (Figure 4a and b) and with (Figure 4c) a GBS component. In particular, data
240 from Hansen et al. (2011) and a related study (Wang et al. 2010) argue for a broader range of grain-
241 size sensitive deformation than can be achieved with a simple combination of diffusion creep and
242 dislocation creep. (Discrepancies among datasets associated with diffusion creep are discussed in
243 section 2.4.)

244 The source of grain-size sensitivity during GBS is not well understood. Classic models for sliding
245 associated with dislocation motion stem from work on superplastic metals and ceramics (e.g.,
246 Langdon 2009), in which sliding is presumed to contribute significantly to the total strain and n_{GBS}
247 ≤ 2. However, a variety of materials exhibit values of $n_{GBS} > 2$ in conjunction with a measurable
248 grain-size sensitivity (Hahn & Averback 1991, Langdon & Vastava 1982). In this regime, direct
249 measurements of grain-boundary offsets reveal that, although sliding occurs, it contributes
250 relatively little to the overall strain (1–10%, Langdon 2006). Instead, interaction between lattice

dislocations and grain boundaries, rather than sliding itself, is inferred to cause grain-size sensitivity. For olivine, Platt and Behr (2011) derived a model in which grain-boundary migration annihilates dislocations and results in $n_{GBS} = 3$ and $p_{GBS} = 1$. Alternatively, Ferreira et al. (2021) used microstructural observations to suggest that dislocations climb into grain boundaries, which both induces sliding and limits the overall strain rate. Finally, Breithaupt et al. (2020) incorporated dislocation climb into grain boundaries to derive a model that yields a steady-state solution with $n_{gbs} = 3$ and $p_{gbs} = 1$ (Figure 4).

The importance of GBS for hydrous olivine is subject to debate. Hirth & Kohlstedt (2003) found no evidence for a grain-size dependence in the experiments of Mei & Kohlstedt (2000), but the grain-size range (18–25 μm) may have been insufficient to detect wet GBS. Ohuchi et al. (2015) argued for the occurrence of wet GBS by combining results from wet (2–4 μm grain sizes) and dry (1–10 μm grain sizes) deformation-DIA experiments at normalized conditions, but relatively few experiments were available to test their hypothesis. Hirth & Kohlstedt (2003) suggested that dislocation climb is fast enough under hydrous conditions that strain produced directly by climb (e.g., Nabarro 1967) outpaces processes associated with grain-boundary sliding. Alternatively, if strain rate is limited by dislocation climb into grain boundaries, then the presence of hydrogen may disproportionately influence the rate of recovery at grain boundaries, modifying the conditions at which GBS is dominant.

2.4. Diffusion creep

Since the diffusion creep flow law of Hirth & Kohlstedt (1995a, 2003), several updates have been published (Faul & Jackson 2007, 2011, Yabe et al. 2020, Zhao et al. 2019, Zimmerman &

Kohlstedt 2004). These updates are complex and not always in agreement, indicating that aspects of this mechanism are poorly understood despite extensive experimental work (Figure 4). Some discrepancies originate from compositional variations among experiments, particularly the presence of secondary phases and impurities, which promote processes such as phase-boundary sliding (Zhao et al. 2019) and interface-controlled creep (Yabe et al. 2020). Other discrepancies reflect differences in experimental setup and analytical technique.

2.4.1. Influence of composition on diffusion creep

Compositional differences, particularly secondary mineral phases and trace-element impurities, are a major source of variations among diffusion-creep experiments (Figure 4). The flow law of Hirth & Kohlstedt (1995a, 2003) is similar to flow laws based on multiphase experiments (Zhao et al. 2019, Zimmerman & Kohlstedt 2004), but significantly weaker than flow laws determined using synthetic material (Faul & Jackson 2007, Yabe et al. 2020). Hirth & Kohlstedt (1995a) used powdered natural San Carlos olivine xenocrysts, which have typical upper-mantle compositions (e.g., Frey & Prinz 1978). Zimmerman & Kohlstedt (2004) reported a similar flow law for experiments that used a powdered lherzolite xenolith. In contrast, Faul & Jackson (2007) determined a flow law that is orders of magnitude stronger at lithospheric conditions, based on experiments using synthetic olivine grown by solution gelation, which produces fine-grained samples that are melt- and water-free.

Experiments specifically targeting multiphase behavior have yielded conflicting results. Weakening relative to olivine-only deformation was observed in experiments on natural olivine mixed with orthopyroxene (Sundberg & Cooper 2008) or with clinopyroxene (Zhao et al. 2019). Both studies suggested that secondary phases lead to faster strain rates through phase-boundary

sliding and reactions. However, weakening was not observed in experiments on forsterite mixed with enstatite (Tasaka et al. 2013) or San Carlos olivine mixed with ferropericlase (Wiesman et al. 2018). A complicating factor in comparing multiphase experiments to olivine-only experiments is that multiphase deformation promotes the formation of finer-grained aggregates (e.g., Farla et al. 2013). Thus comparison of olivine-only versus multiphase experiments requires normalization of data using a presumed grain-size dependence.

The presence of very small melt fractions in the nominally melt-free experiments of Hirth & Kohlstedt (1995a) was suggested as a reason for the lower viscosity of this flow law, as Faul & Jackson (2007) argued that melt provides significantly faster pathways for diffusion even at melt fractions <1%. Theoretical analysis by Takei & Holtzman (2009) suggested that <1% melt can reduce viscosity by a factor of 5 based on a model of spherical grains with circular contact patches. However, subsequent analysis using a more realistic geometry of truncated octahedrons suggests that small amounts of melt provide only a factor of 1.4 viscosity reduction (Rudge 2018).

Some studies (e.g., Jain et al. 2019, Karato et al. 1986) have proposed a grain-size exponent of $p_{diff} = 2$ (i.e., lattice diffusion; Figure 2) instead of $p_{diff} = 3$ (i.e., grain-boundary diffusion). The analysis of Jain et al. (2019), based on inversion of several published experimental datasets, is difficult to reconcile with the observation that strain rates calculated from the diffusivity of Si along olivine grain boundaries (Fei et al. 2016) agree with experimental determinations of diffusion creep rates (Yabe et al. 2020). This discrepancy may reflect the dependence of the inversion on estimates of experimental errors and interlab bias, which are often under-constrained. Existing datasets may also not provide enough constraints on all aspects of diffusion creep. The analysis by Jain et al. (2019) hinted at a regime with $p_{diff} = 1$, implying interface-controlled creep, but this regime was excluded from subsequent evaluation due to a lack of data.

2.4.2. The role of interface-controlled creep

Perhaps the most important development for understanding diffusion creep is the recent exploration of interface-controlled creep in experiments by Hiraga and co-authors (e.g., Hiraga et al. 2010, Miyazaki et al. 2013, Tasaka et al. 2013, Yabe et al. 2020). Experiments on fine-grained olivine aggregates demonstrate a transition in creep behavior at low stress (Yabe et al. 2020), which suggests that diffusion creep is a serial combination of interface-controlled creep and grain-boundary diffusion creep (Figure 3). During grain-boundary diffusion creep, grain boundaries are assumed to be perfect sources and sinks for vacancies (e.g., Coble 1963). In interface-controlled creep, the interface reaction to move ions or their vacancies into grain boundaries becomes the rate-limiting step at very low stresses (e.g., Raj & Ashby 1971). Arzt et al. (1983) suggested that this process could alternatively be visualized as drag from impurities on the grain-boundary dislocations that produce sliding. In the interface-controlled regime, $n_{diff} = 2$ or 3 and $p_{diff} = 1$, compared to $n_{diff} = 1$ and $p_{diff} = 3$ for the grain-boundary diffusion regime (Arzt et al. 1983, Yabe et al. 2020).

The experiments by Yabe et al. (2020) demonstrate that diffusion creep rates are enhanced at near-solidus conditions in the presence of typical impurities, such as Ca and Al, in olivine. Their measurements indicate the possible importance of grain-boundary processes such as grain-boundary disordering (e.g., Cantwell et al. 2020). However, direct application of these flow laws is difficult: (1) The interface-controlled regime scales with solidus temperature, which is pressure-dependent, so additional constraints are needed for the interdependent variables in the flow law. (2) As 10–30 vol% pyroxene formed during doped experiments (Yabe et al. 2020), pyroxene must contain most of the Ca and Al in these experiments and olivine is thus under-saturated relative to typical mantle abundances (10s–100s ppm Al and Ca, De Hoog et al. 2010). (3) The presence of

pyroxene raises the possibility that weakening also occurred due to phase-boundary sliding. As discussed above, some previous diffusion creep experiments on olivine-pyroxene mixtures have attributed weakening to reactions and sliding associated with interphase boundaries (Sundberg & Cooper 2008, Zhao et al. 2019).

2.4.3. Uncertainties associated with grain size

Grain-size analysis has several sources of uncertainty (see sidebar on Grain-Size Analysis). The smallest population of grains may be undercounted if measurements are not made with sufficient resolution. The flow laws of Hansen et al. (2011) and Hirth & Kohlstedt (1995a) were conducted at very similar conditions but exhibit more than a factor of 10 difference in strain rate (Figure 3 and Figure 4). Hansen et al. (2011, see their appendix B) suggested that this difference results from errors in grain-size measurement. They concluded that the smallest grains were undercounted in the original experiments, though Zhao et al. (2019, see their appendix B) suggested a lower size threshold at which undercounting is a problem. This uncertainty is significant because undercounting of the smallest grains leads to a flow law appearing weaker than it actually is. This discrepancy remains to be resolved.

2.4.4. Which diffusion creep flow law is applicable to the lithospheric mantle?

Much work remains to be done to clarify our understanding of diffusion creep, but we seek to make a practical recommendation based on the available data. In Table 1, we recommend two versions of the diffusion creep flow law: HK03 from Hirth & Kohlstedt (2003) and HZK11, which uses the revised value of A_{diff} from Hansen et al. (2011, see their appendix A). The similarity of the HK03 flow law to multiphase deformation (see section 2.7) suggests that this flow law reasonably captures the behavior of peridotite during diffusion creep in the mantle. The flow law

363 from HZK11 may be better suited for deformation not affected by secondary phases and for
364 analysis of deformation in combination with the GBS flow law, which is derived from the same
365 dataset (Figure 4c).

366 These uncertainties in the diffusion creep flow law are relatively unimportant for understanding
367 lithospheric strength outside of shear zones, which is mainly composed of coarse-grained
368 peridotite (Figure 1). Average olivine grain sizes of protogranular and porphyroclastic peridotites
369 range from ~0.5 to 1.5 mm (e.g., Achenbach et al. 2011, Kumamoto et al. 2019, Mercier & Nicolas
370 1975). As illustrated in Figure 5, these grain sizes are too large for diffusion creep to be an
371 important mechanism for accommodating flow, and bulk lithospheric strength is dependent on
372 flow laws for dislocation-based mechanisms.

373 At plate boundary-scale shear zones (Figure 1), diffusion creep becomes the major mechanism for
374 accommodating motion in the crust and mantle (e.g., Fossen & Cavalcante 2017, Vauchez et al.
375 2012). Analyses of peridotite mylonites from transform faults indicate that these shear zones are
376 compositionally complex systems, with the smallest (<10 μm) olivine grains intermixed with
377 other, often hydrous, phases (e.g., Kohli & Warren 2020). This observation suggests that the flow
378 law for wet diffusion creep is the most applicable for modeling mantle shear zones, as illustrated
379 in Figure 6.

380

381 ### *2.5. Wet flow laws*

382 Flow laws for olivine containing hydrogen ("wet flow laws") are important for deformation in
383 shear zones, for which observations of natural peridotites suggest that hydration is associated with

grain-size reduction and the transition to diffusion creep (e.g., Kohli et al. 2021, Precigout et al. 2017). In the rest of the lithosphere, most of the mantle is dry as hydrogen is lost during melting to form the crust at mid-ocean ridges (e.g., Hirschmann 2006, Hirth & Kohlstedt 1996). However, percolation of fluids and melts can lead to subsequent rehydration of the lithosphere, particularly in continental cratons (e.g., Demouchy & Bolfan-Casanova 2016, Peslier 2010).

The original wet flow laws for olivine were derived using hydrogen concentrations determined by Fourier transform infrared spectroscopy prior to the updated calibration published by Bell et al. (2003). This study found that previously reported concentrations are too high by a factor of 2.3–3.5, with the exact factor depending on the analytical setup. As pointed out by Hirth & Kohlstedt (2003), updating the water content of wet deformation experiments does not change the creep rate dependence on water content, but it does change the pre-exponential factor. Experimental studies have often used unpolarized radiation to analyze oriented crystals, for which Bell et al. (2003) suggest a correction factor (β) of 3.5. We used this value and the relationship $c_{\mathrm{OH}}^{\mathrm{updated}} = \beta c_{\mathrm{OH}}^{\mathrm{original}}$ to update the pre-exponential terms for dislocation and diffusion creep in Table 1 according to

$$A^{\mathrm{updated}} \left(\beta c_{\mathrm{OH}}^{\mathrm{original}}\right)^{r} = A^{\mathrm{original}} \left(c_{\mathrm{OH}}^{\mathrm{original}}\right)^{r}. \tag{5}$$

The wet flow laws are typically implemented as an alternative to the dry flow laws, however, when extrapolated to low water concentrations, the wet flow laws eventually become stronger than the dry flow laws. A material at low water content will appear artificially strong if only the wet flow laws are used, but a microphysical model for the transition from wet to dry deformation is not available. As a practical solution, we suggest taking the total strain rate as a summation of the wet and dry flow laws, but this represents an approximation as it does not maintain charge neutrality.

2.6. Flow laws for other mantle minerals

Pyroxene deformation is important for constraining lithospheric strength as the shallow upper mantle is composed of orthopyroxene (~20%) and clinopyroxene (~4%), in addition to olivine (~74%). An aluminous phase (spinel or garnet) is also present, but is volumetrically unimportant in most of the lithospheric mantle.

Limited experimental constraints are available for orthopyroxene deformation, partly due to the narrow range of conditions over which experiments can be conducted without a transition to clinoenstatite or protoenstatite polymorphs. Experiments by Lawlis (1998) indicate that orthoenstatite deforms by two mechanisms, interpreted as diffusion creep at low stress and dislocation creep at high stress. Bystricky et al. (2016) used these experiments to calibrate a dislocation-creep flow law for orthoenstatite (Table 1). They observed that orthoenstatite is two times stronger than olivine at high stress and ~1200°C, but that the strength of orthopyroxene may be similar to olivine as temperature increases and stress decreases. The effects of external conditions (water and oxygen fugacities, melt content, and silica activity) are unconstrained and may substantially change the rheology of orthopyroxene relative to olivine. Bruijn & Skemer (2014) demonstrated that the diffusion creep in orthopyroxene also occurred in the experiments of Lawlis (1998). Although precise constraints on flow-law parameters are not available, their analysis indicates that grain-size sensitive deformation of orthopyroxene can occur at lithospheric conditions when the average grain size is <150 μm.

Flow laws for dry and wet dislocation creep of clinopyroxene are constrained by experiments on natural clinopyroxenite (Bystricky & Mackwell 2001, Chen et al. 2006, Hier-Majumder et al. 2005). These indicate that clinopyroxene is relatively strong, with a relatively high activation

energy (Table 1). Incorporation of hydrogen into clinopyroxene results in significant weakening, such that clinopyroxene can be weaker than olivine at water-saturated conditions (Hier-Majumder et al. 2005). Grain size reduction also results in weakening of clinopyroxene, indicating activation of a grain boundary sliding mechanism (Bystricky & Mackwell 2001).

2.7. Multiphase flow laws

The mantle is polymineralic and individual mineral flow laws provide only an approximation of lithospheric strength. Experimental measurements of multiphase flow laws are difficult as the pressure-temperature range for experiments is limited by the reduced solidus temperature compared to end-member phases. Most studies have explored deformation in the diffusion creep and GBS regimes (e.g., Farla et al. 2013, Ji et al. 2001, McDonnell et al. 2000, Tasaka et al. 2013), which are easier to access at laboratory strain rates. An alternative option is to use theoretical models for multiphase deformation based on flow laws for end-members (e.g., Gardner et al. 2019, Huet et al. 2014, Ji et al. 2003). However, these models do not yet account for some exceptional behavior observed in experiments. For example, the presence of pyroxene in olivine experiments can lead to increased creep rates, potentially due to enhancement of diffusivities by relaxing flux coupling (Sundberg & Cooper 2008), pinning of olivine grain size (Tasaka et al. 2013, 2017, 2020), or phase-boundary sliding (Zhao et al. 2019). These complex interactions between phases, including the influence of second-phase composition, makes it difficult to robustly derive a multiphase flow law. Based on the similarity between the Hirth & Kohlstedt (1995a) dataset and multiphase datasets (Figure 4), we conclude that the HK03 flow law (Table 1) provides the closest approximation for multiphase deformation in the diffusion creep regime.

3. Extrapolation to geological conditions

3.1. Constraints from natural samples

Application of laboratory-derived flow laws to naturally deformed rocks (Figure 7) requires extrapolations in strain rate — from laboratory rates of ~10^{-4}–10^{-6} s^{-1} to lithospheric rates of ~10^{-12}–10^{-16} s^{-1} — and at least one other parameter (temperature, grain size, stress). For diffusion creep, stresses and grain sizes are similar, but experiments are typically conducted at temperatures of ~1100–1300°C, whereas deformation in natural samples occurs down to temperatures of ~600°C (Jaroslow et al. 1996). For GBS and dislocation creep, stresses in experiments are >100 MPa, whereas stresses in natural samples are closer to 10 MPa (e.g., Linckens et al. 2011). Grain sizes in experiments are typically 1-100 μm, but GBS in natural samples likely occurs at grain sizes >100 μm (Hansen & Warren 2015). In addition, experiments are typically on monophase aggregates with a total sample diameter limited to ≲30 mm.

Testing of flow laws against naturally deformed rocks is an important step for evaluating the applicability of laboratory datasets (Figure 5 and Figure 6). Samples from ductile shear zones are useful for this validation (e.g., Hirth et al., 2001), as structures and compositions related to deformation are typically preserved in these outcrops. In contrast, samples that undergo lower-strain deformation are harder to interpret as structural features (foliation and lineation) are often not visible and temperatures are hard to constrain if mineral compositions are not reset by the deformation. In shear-zone samples, deformation mechanisms are identified from microstructural analysis (Figure 7) and compared to deformation mechanism maps calculated at conditions constrained by the samples (Figure 6). This approach was applied by Warren & Hirth (2006) to

validate the extrapolation of olivine flow laws to tectonic conditions through analysis of peridotite mylonites from oceanic transform faults.

The mechanisms active during deformation of naturally deformed peridotites are determined from optical and electron microscopy analysis of microstructures (Figure 7). Many studies focus on crystallographic preferred orientations, which are used to infer slip system activity (e.g., Skemer & Hansen 2016). Traditionally, the presence of a crystallographic preferred orientation is taken as an indication that most of the strain results from dislocation glide, while its absence is interpreted as indicative of diffusion creep. However, crystallographic alignment has been observed in some diffusion creep experiments, though misorientation analysis indicates the absence of dislocation movement within grains (e.g., Miyazaki et al. 2013, Zhao et al. 2019). This observation highlights the importance of detailed interrogation of microstructural datasets to identify the mechanisms that accommodated strain.

No clear microstructural difference has been identified between GBS and dislocation creep (Figure 7), likely because both mechanisms produce strain through dislocation motion and are rate limited by dislocation recovery, so identification of these mechanisms is often based on comparison to flow laws. For example, Hansen & Warren (2015) found evidence for GBS through comparison of olivine viscosity to pyroxene viscosity in co-deformed dunite/harzburgite pairs. In contrast, low-temperature plasticity appears to have unique microstructural features (e.g., Druiventak et al. 2011), such as deformation bands that have been observed in both natural (Matysiak & Trepmann 2012) and experimental (Wallis et al. 2020) samples (Figure 7).

Very few studies of naturally deformed peridotites provide independent constraints on flow laws due to the difficulty of quantifying conditions (temperature, pressure, stress, and strain rate) at the

492 time of deformation. By definition, lithospheric deformation occurs at temperatures lower than the
493 mantle potential temperature (≳1300°C), which places an upper limit on temperature. The
494 temperature of deformation is further constrained by geothermometry, which records the closure
495 temperature for a mineral exchange system. This approach is useful for mylonites, which indicate
496 deformation temperatures of ~600-1000°C (Jaroslow et al. 1996, Prigent et al. 2020). However,
497 coarser-grained peridotites that are exhumed slowly (i.e., ridges, ophiolites, massifs) typically
498 record the closure temperature of the exchange system and not the deformation temperature
499 (Dygert & Liang 2015). Even xenoliths, which are quenched from high temperature during
500 eruption, may have their deformation temperature reset by later events (e.g., Chin et al. 2021,
501 Mercier & Nicolas 1975).

502 The pressure of deformation is difficult to constrain for most lithospheric peridotites as the
503 majority come from the spinel-stability field, where mineral exchange reactions have limited
504 pressure sensitivity. In the oceanic lithosphere, the pressure of deformation is instead estimated by
505 combining thermometry with modeling of lithospheric thermal structure to estimate depth (e.g.,
506 Kohli et al. 2021). In the case of garnet-bearing peridotites, the barometer of Brey & Köhler (1990)
507 is typically applied to constrain pressure. Overall, the lack of pressure constraints for natural
508 samples is compensated by the small values of V^* (see sidebar on Activation Volume), which
509 means that the effect of depth on lithospheric strength only becomes significant in the deep
510 continental lithosphere.

511 Stress in naturally deformed samples can be estimated using a piezometer, for which stress applied
512 during deformation is related to the dynamically recrystallized grain or subgrain size (see sidebar
513 on the Relationship Between Stress and Grain Size). Estimates from peridotite mylonites
514 (Figure 6) indicate that stresses are ~10–100 MPa (e.g., Kohli et al. 2021, Linckens et al. 2011).

Estimates for coarser-grained samples, reflecting flow in the lithosphere, are ~1–20 MPa (Behr & Hirth 2014, Hansen & Warren 2015, Linckens et al. 2011), as illustrated in Figure 5 and Figure 6.

Strain rate is one of the most challenging parameters to constrain in rocks, particularly in peridotites, which have low concentrations of many trace elements and isotopes that could be used to provide relative (e.g., diffusion chronometry) or absolute (e.g., radiometric) time constraints. Instead, strain rates have been estimated using olivine flow laws combined with temperature, grain size, and piezometry-based stress estimates (e.g., Behr & Hirth 2014, Warren & Hirth 2006). In active shear zones, plate velocity can be combined with deformation zone width to provide an independent estimate of strain rate. For example, at oceanic transform faults (Figure 6), this leads to a strain rate estimate of 10^{-10}–10^{-14} s^{-1} (Warren & Hirth 2006). However, if only a sub-region of a shear zone is active at any given time, these estimates represent a lower bound on strain rate and deformation may have been faster.

3.2. Comparison to geophysical observations

The olivine flow laws provide predictions for lithospheric strength that can be compared to geophysical observations. Here we focus on the oceanic lithosphere because of the well constrained thermal and compositional structure. Figure 8 presents a strength-depth diagram for mature oceanic lithosphere calculated using the geotherm in Figure 1 at a strain rate of 10^{-15} s^{-1} and grain size of 1 mm. We represent ductile deformation using the flow laws in Table 1 and brittle deformation using a model for either the onset of microcracking in intact rock (Baud et al. 2014) or friction for sliding on a mature fault (Byerlee 1978). Under these conditions, the lithosphere is predicted to initially yield by crystal plasticity at depths ≥20 km. If deformation continues, strain hardening will lead to frictional sliding above 35 km or steady-state crystal-plasticity below 35

537 km. Crystal-plastic deformation is controlled by low-temperature plasticity at the shallowest
538 depths and transitions to GBS at ~45 km. Diffusion creep dominates below ~90 km, however our
539 calculation is for static grain size and does not account for increased grain size with depth predicted
540 by grain-size evolution models (Behn et al. 2009), which would instead lead to dislocation creep
541 at depth. Our flow law predictions are generally consistent with the time-dependent model of
542 Breithaupt et al. (2020), although the promotion of pipe diffusion due to high dislocation densities
543 predicts slightly lower stresses between 35 and 50 km. The model of Gouriet et al. (2019) predicts
544 a much weaker lithosphere, potentially due to underpredicting the magnitude of strain hardening
545 (compare to Figure 3).

546 In Figure 8b, we compare our calculated strength profiles to effective elastic thicknesses estimated
547 by lithospheric flexure near seamounts/islands (Watts et al. 2013) and at subduction zones (Hunter
548 & Watts 2016). We use the intersections between brittle and ductile mechanisms to define a depth
549 range for the brittle-ductile transition (gray region, cf., Meyer et al. 2019), which roughly
550 corresponds with predicted elastic thicknesses, as well as the maximum depth of earthquake
551 nucleation in the oceanic lithosphere (e.g., Richards et al. 2020). As elastic thickness is taken to
552 be a measure of plate strength (e.g., Burov 2011), the integrated strength predicted from these
553 values should agree with integrated strength calculated from the strength-depth profile. However,
554 as pointed out in several recent studies (Bellas et al. 2020, Hunter & Watts 2016, Zhong & Watts
555 2013) and as highlighted in Figure 8c, estimates of the integrated strength from plate flexure and
556 from other estimates of stress state are all lower than predicted by the steady-state flow laws and—
557 in most cases—lower than the initial strength at yield. Weaker flow laws such as that from Gouriet
558 et al. (2019) result in integrated strengths closer to geophysical estimates, but also predict a brittle-
559 ductile transition far shallower (~15 km at 80 Myr) than the depth extent of oceanic earthquakes

(≤50 km, Craig et al. 2014). The discrepancy between flow laws and observations of lithospheric strength remains one of the key targets for future research (cf., Bellas et al. 2022).

4. Future directions

Examining grain-size sensitive creep: Existing diffusion creep flow laws make very different predictions about lithospheric strength (Figure 3 and Figure 4), while the limited data for wet GBS makes its role in lithospheric deformation uncertain. Experiments are needed across a wider range of grain sizes and trace element abundances in these regimes to resolve differences among existing datasets by exploring grain-size dependency and interface-controlled creep. These effects are important for modeling shear zones and for predicting transitions in mechanisms deep in the lithosphere, particularly in regions where rehydration may occur.

Constraining multiphase deformation: The presence of additional phases modifies the response of olivine to deformation, due to physical behavior (phase mixing, phase boundary sliding, dynamic recrystallization) and chemical processes (reactions, diffusion pathways). Some processes depend on the specific secondary phase that is present, which determines the viscosity contrast between phases and the reaction behavior of the system. All these processes are modified by the presence of water and other fluids during deformation. In addition, almost no experiments have been conducted on olivine + orthopyroxene outside of the diffusion creep regime, yet this lithology (i.e., harzburgite) dominates the lithospheric mantle.

Reconciling with geophysical observations: The discrepancy between lithospheric strength predicted by experimental data compared to geophysical observations (Figure 8) remains a major

challenge. More geophysical measurements are needed, including ones that complement flexural analysis, and more data are needed in the oceans, where the strength of the lithospheric mantle can be constrained without the complexity of continental crust. Most of the strength-bearing portion of the lithosphere is in the brittle-ductile transition, which has the most complex behavior and is the least constrained.

Strength of the brittle/ductile transition: This part of the lithosphere is the region of highest strength, but also the region of greatest uncertainty. The depth of the transition is not fixed, as its location depends on strain rate, grain size, and thermal structure (Figure 1). Numerous studies have suggested that brittle and ductile processes are both active in this region (Figure 8), but the interplay of these processes is not well understood. Key areas of uncertainty include the role of localized versus distributed deformation, strain hardening during low-temperature plasticity, effects of transiently high stresses and strain rate during the seismic cycle, and the importance of brittle processes for grain-size reduction and phase mixing.

5. Summary Phrases

- Ductile deformation of the lithospheric mantle is constrained by experimental data for olivine.
- Olivine deforms by four major mechanisms: low-temperature plasticity, dislocation creep, dislocation-accommodated grain-boundary sliding, and diffusion creep.
- Observations of naturally deformed rocks are consistent with extrapolation of olivine flow laws from experimental conditions.

- Experiments predict stronger lithosphere than geophysical observations, likely due to gaps in constraints on deformation in the brittle-ductile transition.

6. Acknowledgements

We thank Greg Hirth, David Kohlstedt, Thomas Breithaupt, Takehiko Hiraga, Cécile Prigent, and Ningli Zhao for fruitful discussions during manuscript preparation. This manuscript benefited from comments by David Kohlstedt and an anonymous reviewer. We are grateful to Margaret Boettcher for calculating transform fault geotherms. EBSD datasets used to make Figure 7 were kindly provided by Emily Chin, Florian Heidelbach, Claudia Trepmann, David Wallis, and Ningli Zhao, along with our unpublished datasets. This material is based upon work supported by the National Science Foundation under grants OCE-1832868 and EAR-2113408 to J.M.W. and EAR-2022433 to L.N.H.

7. Literature Cited

Abercrombie RE, Ekström G. 2001. Earthquake slip on oceanic transform faults. Nature. 410(6824):74–77

Achenbach KL, Cheadle MJ, Faul UH, Kelemen PB, Swapp SM. 2011. Lattice-preferred orientation and microstructure of peridotites from ODP Hole 1274A (15°39·N), Mid-Atlantic Ridge: Testing models of mantle upwelling and tectonic exhumation. Earth Planet. Sci. Lett. 301(1):199–212

Arzt E, Ashby MF, Verrall RA. 1983. Interface Controlled Diffusional Creep. Acta Metall. 31(12):1977–89

Austin NJ, Evans B. 2007. Paleowattmeters: A scaling relation for dynamically recrystallized grain size. Geology. 35(4):343

Bai Q, Kohlstedt DL. 1992. High-temperature creep of olivine single crystals. II: Dislocation structures. Tectonophysics. 206(1-2):1–29

Bai Q, Mackwell SJ, Kohlstedt DL. 1991. High-temperature creep of olivine single crystals 1. Mechanical results for buffered samples. J. Geophys. Res. 96(B2):2441–63

Baud P, Wong T-F, Zhu W. 2014. Effects of porosity and crack density on the compressive strength of rocks. Int. J. Rock Mech. Min. Sci. 67:202–11

Behn MD, Boettcher MS, Hirth G. 2007. Thermal structure of oceanic transform faults. Geology. 35(4):307–10

Behn MD, Hirth G, Elsenbeck JR II. 2009. Implications of grain size evolution on the seismic structure of the oceanic upper mantle. Earth Planet. Sci. Lett. 282(1-4):178–89

Behr WM, Hirth G. 2014. Rheological properties of the mantle lid beneath the Mojave region in southern

635 California. Earth Planet. Sci. Lett. 393:60–72

636 Bellas A, Zhong S, Watts A. 2020. Constraints on the rheology of the lithosphere from flexure of the
637 pacific plate at the Hawaiian islands. Geochem. Geophys. Geosyst. 21(2):e2019GC008819

638 Bellas A, Zhong S, Watts AB. 2022. Reconciling lithospheric rheology between laboratory experiments,
639 field observations and different tectonic settings. Geophys. J. Int. 228(2):857–75

640 Bell DR, Rossman GR, Maldener J, Endisch D, Rauch F. 2003. Hydroxide in olivine: A quantitative
641 determination of the absolute amount and calibration of the IR spectrum. J. Geophys. Res.
642 108(B2):1–9

643 Billen MI. 2008. Modeling the Dynamics of Subducting Slabs. Annu. Rev. Earth Planet. Sci. 36:325–56

644 Boettcher MS, Hirth G, Evans B. 2007. Olivine friction at the base of oceanic seismogenic zones. J.
645 Geophys. Res. 112:B01205

646 Bollinger C, Marquardt K, Ferreira F. 2019. Intragranular plasticity vs. grain boundary sliding (GBS) in
647 forsterite: microstructural evidence at high pressures (3.5-5.0 GPa). Am. Mineral. in press:1–48

648 Boneh Y, Wallis D, Hansen LN, Krawczynski MJ, Skemer P. 2017. Oriented grain growth and
649 modification of “frozen anisotropy” in the lithospheric mantle. Earth Planet. Sci. Lett. 474:368–74

650 Brace WF, Byerlee JD. 1966. Recent Experimental Studies Of Brittle Fracture Of Rocks, Vol. 8.
651 OnePetro

652 Brantut N, Heap MJ, Meredith PG, Baud P. 2013. Time-dependent cracking and brittle creep in crustal
653 rocks: A review. J. Struct. Geol. 52:17–43

654 Breithaupt T, Hansen LN, Kumamoto KM, Katz RF. 2020. Dislocation density evolution and its
655 consequences for steady-state and transient creep. New theory and models. . 2020:MR022–0009

Brey GP, Kohler TP. 1990. Geothermobarometry in four-phase lherzolites II. New thermobarometers, and practical assessment of existing thermobarometers. J. Petrol. 31(6):1353–78

Bruijn RHC, Skemer P. 2014. Grain-size sensitive rheology of orthopyroxene. Geophys. Res. Lett. 41(1):4894–4903

Bürgmann R, Dresen G. 2008. Rheology of the Lower Crust and Upper Mantle: Evidence from Rock Mechanics, Geodesy, and Field Observations. Annu. Rev. Earth Planet. Sci. 36(1):531–67

Burov EB. 2011. Rheology and strength of the lithosphere. Marine and Petroleum Geology. 28(8):1402–43

Byerlee J. 1978. Friction of Rocks. In Rock Friction and Earthquake Prediction, eds. JD Byerlee, M Wyss, pp. 615–26. Basel: Birkhäuser Basel

Bystricky M, Lawlis J, Mackwell SJ, Heidelbach F, Raterron P. 2016. High-temperature deformation of enstatite aggregates. J. Geophys. Res. 121(9):6384–6400

Bystricky M, Mackwell SJ. 2001. Creep of dry clinopyroxene aggregates. J. Geophys. Res. 106(B7):13443–54

Cantwell PR, Frolov T, Rupert TJ, Krause AR, Marvel CJ, et al. 2020. Grain boundary complexion transitions. Annu. Rev. Mater. Res. 50(1):465–92

Carter NL. 1976. Steady State Flow of Rocks. Rev. Geophys. Space Phys. 14(3):301

Chen S, Hiraga T, Kohlstedt DL. 2006. Water weakening of clinopyroxene in the dislocation creep regime. J. Geophys. Res. 111(B8):1–14

Chin EJ, Chilson-Parks B, Boneh Y, Hirth G, Saal AE, et al. 2021. The peridotite deformation cycle in cratons and the deep impact of subduction. Tectonophysics. 817:229029

677 Coble RL. 1963. A model for boundary diffusion controlled creep in polycrystalline materials. J. Appl.
678 Phys. 34(6):1679–82

679 Cottrell E, Birner SK, Brounce M, Davis FA, Waters LE, Kelley KA. 2022. Oxygen Fugacity Across
680 Tectonic Settings. In Geophysical Monograph Series, eds. R Moretti, DR Neuville, pp. 33–61.
681 Wiley. 1st ed.

682 Craig TJ, Copley A, Jackson JA. 2014. A reassessment of outer-rise seismicity and its implications for the
683 mechanics of oceanic lithosphere. Geophys. J. Int. 197(1):63–89

684 De Hoog JCM, Gall L, Cornell DH. 2010. Trace-element geochemistry of mantle olivine and application
685 to mantle petrogenesis and geothermobarometry. Chem. Geol. 270(1-4):196–215

686 Demouchy S. 2021. Defects in olivine. Eur. J. Mineral. 33(3):249–82

687 Demouchy S, Bolfan-Casanova N. 2016. Distribution and transport of hydrogen in the lithospheric
688 mantle: A review. Lithos. 240:402–25

689 Dieterich JH. 2007. Applications of Rate- and State-Dependent Friction to Models of Fault-Slip and
690 Earthquake Occurrence. In Earthquake Seismology, Vol. 4, ed. G Schubert, pp. 107–29

691 Dixon NA, Durham WB. 2018. Measurement of activation volume for creep of dry olivine at upper-
692 mantle conditions. J. Geophys. Res. 123(10):8459–73

693 Dorn JE. 1955. Some fundamental experiments on high temperature creep. J. Mech. Phys. Solids.
694 3(2):85–116

695 Druiventak A, Matysiak A, Renner J, Trepmann CA. 2011. Kick-and-cook experiments on peridotite:
696 simulating coseismic deformation and post-seismic creep. Terra Nova. 24(1):62–69

697 Durham WB, Goetze C, Blake B. 1977. Plastic flow of oriented single crystals of olivine 2. Observations

698 and interpretations of the dislocation structures. J. Geophys. Res. 82(36):5755–70

699 Dygert NJ, Liang Y. 2015. Temperatures and cooling rates recorded in REE in coexisting pyroxenes in
700 ophiolitic and abyssal peridotites. Earth Planet. Sci. Lett. 420:151–61

701 England P, Molnar P. 2015. Rheology of the lithosphere beneath the central and western Tien Shan. J.
702 Geophys. Res. [Solid Earth]. 120(5):2014JB011733

703 Farla RJM, Karato S-I, Cai Z. 2013. Role of orthopyroxene in rheological weakening of the lithosphere
704 via dynamic recrystallization. Proceedings of the National Academy of Sciences. 110(41):16355–60

705 Faul UH, Fitz Gerald JD, Farla RJM, Ahlefeldt R, Jackson I. 2011. Dislocation creep of fine-grained
706 olivine. J. Geophys. Res. 116(B1):B01203

707 Faul UH, Jackson I. 2007. Diffusion creep of dry, melt-free olivine. J. Geophys. Res. 112(B4):B04204

708 Faul UH, Jackson I. 2015. Transient creep and strain energy dissipation: An experimental perspective.
709 Annu. Rev. Earth Planet. Sci. 43(1):541–69

710 Fei H, Hegoda C, Yamazaki D, Wiedenbeck M, Yurimoto H, et al. 2012. High silicon self-diffusion
711 coefficient in dry forsterite. Earth Planet. Sci. Lett. 345:95–103

712 Fei H, Koizumi S, Sakamoto N, Hashiguchi M, Yurimoto H, et al. 2016. New constraints on upper mantle
713 creep mechanism inferred from silicon grain-boundary diffusion rates. Earth Planet. Sci. Lett.
714 433:350–59

715 Fei H, Wiedenbeck M, Yamazaki D, Katsura T. 2013. Small effect of water on upper-mantle rheology
716 based on silicon self-diffusion coefficients. Nature. 498(7453):213–15

717 Ferreira F, Hansen LN, Marquardt K. 2021. The Effect of Grain Boundaries on Plastic Deformation of
718 Olivine. J. Geophys. Res. [Solid Earth]. 126(7):e2020JB020273

719 Fischer KM, Rychert CA, Dalton CA, Miller MS, Beghein C, Schutt DL. 2020. A comparison of oceanic
720 and continental mantle lithosphere. Phys. Earth Planet. Inter. 309:106600

721 Fossen H, Cavalcante GCG. 2017. Shear zones – A review. Earth-Sci. Rev. 171:434–55

722 Freed AM, Hirth G, Behn MD. 2012. Using short-term postseismic displacements to infer the ambient
723 deformation conditions of the upper mantle. J. Geophys. Res. 117(B1):B01409

724 Frey FA, Prinz M. 1978. Ultramafic inclusions from San Carlos, Arizona: Petrologic and geochemical
725 data bearing on their petrogenesis. Earth Planet. Sci. Lett. 38:129–76

726 Frost HJ, Ashby MF. 1982. Deformation Mechanism Maps: Plasticity and Creep of Metals and Ceramics.
727 Oxford, UK: Pergamon Press

728 Gardner RL, Piazolo S, Daczko NR, Evans L. 2019. Ductile Deformation Without Localization: Insights
729 From Numerical Modeling. Geochem. Geophys. Geosyst. 139

730 Goddard RM, Hansen LN, Wallis D, Stipp M, Holyoke CW, et al. 2020. A Subgrain-Size Piezometer
731 Calibrated for EBSD. Geophys. Res. Lett. 47(23):e2020GL090056

732 Goldsby DL, Kohlstedt DL. 2001. Superplastic deformation of ice: Experimental observations. J.
733 Geophys. Res. 106(B6):11017–30

734 Gouriet K, Cordier P, Garel F, Thoraval C, Demouchy S, et al. 2019. Dislocation dynamics modelling of
735 the power-law breakdown in olivine single crystals: Toward a unified creep law for the upper
736 mantle. Earth Planet. Sci. Lett. 506:282–91

737 Griggs DT. 1936. Deformation of Rocks under High Confining Pressures: I. Experiments at Room
738 Temperature. J. Geol. 44(5):541–77

739 Hahn H, Averback RS. 1991. Low-temperature creep of nanocrystalline titanium(IV) oxide. J. Am.

740 Ceram. Soc. 74(11):2918–21

741 Hansen LN, Kumamoto KM, Thom CA, Wallis D, Durham WB, et al. 2019. Low-temperature plasticity
742 in olivine: Grain size, strain hardening, and the strength of the lithosphere. J. Geophys. Res.
743 2018JB016736

744 Hansen LN, Wallis D, Breithaupt T, Thom CA, Kempton I. 2021. Dislocation Creep of Olivine:
745 Backstress Evolution Controls Transient Creep at High Temperatures. J. Geophys. Res.
746 126(5):e2020JB021325

747 Hansen LN, Warren JM. 2015. Quantifying the effect of pyroxene on deformation of peridotite in a
748 natural shear zone. J. Geophys. Res. 120(4):2717–38

749 Hansen LN, Zimmerman ME, Kohlstedt DL. 2011. Grain boundary sliding in San Carlos olivine: Flow
750 law parameters and crystallographic-preferred orientation. J. Geophys. Res. 116(B8):B08201

751 Hier-Majumder S, Mei S, Kohlstedt DL. 2005. Water weakening of clinopyroxenite in diffusion creep. J.
752 Geophys. Res. 110(B):B07406

753 Hiraga T, Miyazaki T, Tasaka M, Yoshida H. 2010. Mantle superplasticity and its self-made demise.
754 Nature. 468(7327):1091–94

755 Hirschmann MM. 2006. Water, melting, and the deep earth H_2O cycle. Annu. Rev. Earth Planet. Sci.
756 34:627–53

757 Hirth G, Kohlstedt DL. 1995a. Experimental constraints on the dynamics of the partially molten upper
758 mantle: Deformation in the diffusion creep regime. J. Geophys. Res. 100(B2):1981–2001

759 Hirth G, Kohlstedt DL. 1995b. Experimental constraints on the dynamics of the partially molten upper
760 mantle: 2. Deformation in the dislocation creep regime. J. Geophys. Res. 100(B8):15441–49

761 Hirth G, Kohlstedt DL. 1996. Water in the oceanic upper mantle: implications for rheology, melt
762 extraction and the evolution of the lithosphere. Earth Planet. Sci. Lett. 144(1-2):93–108

763 Hirth G, Kohlstedt DL. 2003. Rheology of the upper mantle and the mantle wedge: A view from the
764 experimentalists. Geophysical Monograph. 138:83–105

765 Hirth G, Kohlstedt DL. 2015. The stress dependence of olivine creep rate: Implications for extrapolation
766 of lab data and interpretation of recrystallized grain size. Earth Planet. Sci. Lett. 418:20–26

767 Hirth G, Teyssier CP, Dunlap WJ. 2001. An evaluation of quartzite flow laws based on comparisons
768 between experimentally and naturally deformed rocks. Int. J. Earth Sci. 90(1):77–87

769 Hoek E, Martin CD. 2014. Fracture initiation and propagation in intact rock – A review. Journal of Rock
770 Mechanics and Geotechnical Engineering. 6(4):287–300

771 Huet B, Yamato P, Grasemann B. 2014. The Minimized Power Geometric model: An analytical mixing
772 model for calculating polyphase rock viscosities consistent with experimental data. J. Geophys. Res.
773 119(4):3897–3924

774 Hunter J, Watts AB. 2016. Gravity anomalies, flexure and mantle rheology seaward of circum-Pacific
775 trenches. Geophys. J. Int. 207(1):288–316

776 Idrissi H, Bollinger C, Boioli F, Schryvers D, Cordier P. 2016. Low-temperature plasticity of olivine
777 revisited with in situ TEM nanomechanical testing. Science Advances. 2(3):e1501671

778 Jain C, Korenaga J, Karato S-I. 2019. Global Analysis of Experimental Data on the Rheology of Olivine
779 Aggregates. J. Geophys. Res. 124(1):310–34

780 Jaroslow GE, Hirth G, Dick HJB. 1996. Abyssal peridotite mylonites: implications for grain-size sensitive
781 flow and strain localization in the oceanic lithosphere. Tectonophysics. 256:17–37

Ji S, Wang Z-C, Wirth R. 2001. Bulk flow strength of forsterite–enstatite composites as a function of forsterite content. Tectonophysics. 341(1-4):69–93

Ji S, Zhao P, Xia B. 2003. Flow laws of multiphase materials and rocks from end-member flow laws. Tectonophysics. 370(1):129–45

Karato S-I. 2021. A Theory of Inter-Granular Transient Dislocation Creep: Implications for the Geophysical Studies on Mantle Rheology. J. Geophys. Res. 126(10):e2021JB022763

Karato S-I, Jung H. 2003. Effects of pressure on high-temperature dislocation creep in olivine. Philos. Mag. 83(3):401–14

Karato S-I, Jung H, Katayama I, Skemer P. 2008. Geodynamic Significance of Seismic Anisotropy of the Upper Mantle: New Insights from Laboratory Studies. Annu. Rev. Earth Planet. Sci. 36:59–95

Karato S-I, Paterson MS, Fitz Gerald JD. 1986. Rheology of synthetic olivine aggregates: Influence of grain size and water. J. Geophys. Res. 91(B8):8151–76

Karato S-I, Toriumi M, Fujii T. 1980. Dynamic recrystallization of olivine single crystals during high-temperature creep. Geophys. Res. Lett. 7(9):649–52

Karato S-I, Wu P. 1993. Rheology of the Upper Mantle: A Synthesis. Science. 260:771–78

Kassner ME. 2015. Fundamentals of Creep in Metals and Alloys. Butterworth-Heinemann

Katayama I, Karato S-I. 2008. Low-temperature, high-stress deformation of olivine under water-saturated conditions. Phys. Earth Planet. Inter. 168(3–4):125–33

Katz RF, Jones DWR, Rudge JF, Keller T. 2022. Physics of Melt Extraction from the Mantle: Speed and Style. Annu. Rev. Earth Planet. Sci. 50(1):annurev – earth – 032320–704

Keefner JW, Mackwell SJ, Kohlstedt DL, Heidelbach F. 2011. Dependence of dislocation creep of dunite

on oxygen fugacity: Implications for viscosity variations in Earth's mantle. J. Geophys. Res. 116(B5):B05201

Kocks UF, Argon AS, Ashby MF. 1975. Thermodynamics and Kinetics of Slip. Prog. Mater Sci. 19:

Kohli A, Wolfson-Schwehr M, Prigent C, Warren JM. 2021. Oceanic transform fault seismicity and slip mode influenced by seawater infiltration. Nat. Geosci. 14(8):606–11

Kohli AH, Warren JM. 2020. Evidence for a Deep Hydrologic Cycle on Oceanic Transform Faults. J. Geophys. Res. 125(2):

Kohlstedt DL, Evans B, Mackwell SJ. 1995. Strength of the lithosphere: Constraints imposed by laboratory experiments. J. Geophys. Res. 100(B9):17587–602

Kohlstedt DL, Hansen LN. 2015. Constitutive equations, rheological behavior, and viscosity of rocks. In Mineral Physics, Vol. 2, ed. G Schubert, pp. 441–72. Oxford: Elsevier. 2nd ed.

Kohlstedt DL, Keppler H, Rubie DC. 1996. Solubility of water in the α, β and γ phases of (Mg,Fe)2SiO4. Contrib. Mineral. Petrol. 123(4):345–57

Kumamoto KM, Hansen LN, Wallis D, Li B-S, Armstrong DEJ, et al. 2021. Water Does Not Influence the Plasticity of Olivine at Low Temperatures. American Geophysical Union Fall Meeting. 2021:MR44A – 04

Kumamoto KM, Thom CA, Wallis D, Hansen LN, Armstrong DEJ, et al. 2017. Size effects resolve discrepancies in 40 years of work on low-temperature plasticity in olivine. Sci Adv. 3(9):e1701338

Kumamoto KM, Warren JM, Hansen LN. 2019. Evolution of the Josephine Peridotite shear zones: 2. Influences on olivine CPO evolution. J. Geophys. Res. 124(12):12763–81

Langdon TG. 2006. Grain boundary sliding revisited: Developments in sliding over four decades. J.

824 Mater. Sci. 41(3):597–609

825 Langdon TG. 2009. Seventy-five years of superplasticity: historic developments and new opportunities. J.
826 Mater. Sci. 44(22):5998

827 Langdon TG, Vastava RB. 1982. An Evaluation of Deformation Models for Grain Boundary Sliding. In
828 Mechanical Testing for Deformation Model Development, Vol. 765, eds. RW Rhode, JC
829 Swearengen, pp. 435–51. ASTM International

830 Lawlis JD. 1998. High temperature creep of synthetic olivine-enstatite aggregates. Pennsylvania State
831 University

832 Linckens J, Herwegh M, Müntener O, Mercolli I. 2011. Evolution of a polymineralic mantle shear zone
833 and the role of second phases in the localization of deformation. J. Geophys. Res. 116(B6):B06210

834 Mainprice D, Silver PG. 1993. Interpretation of SKS-waves using samples from the subcontinental
835 lithosphere. Phys. Earth Planet. Inter. 78(3-4):

836 Marone C. 1998. Laboratory-derived friction laws and their application to seismic faulting. Annu. Rev.
837 Earth Planet. Sci. 26:643–96

838 Martinod J, Molnar P. 1995. Lithospheric folding in the Indian Ocean and the rheology of the oceanic
839 plate. Bulletin de la Société Géologique de France. 166(6):813–21

840 Maruyama G, Hiraga T. 2017. Grain- to multiple-grain-scale deformation processes during diffusion
841 creep of forsterite plus diopside aggregate: 1. Direct observations. J. Geophys. Res. 122(8):5890–
842 5915

843 Matysiak AK, Trepmann CA. 2012. Crystal–plastic deformation and recrystallization of peridotite
844 controlled by the seismic cycle. Tectonophysics. 530-531:111–27

McDonnell RD, Peach CJ, van Roermund HLM, Spiers CJ. 2000. Effect of varying enstatite content on the deformation behavior of fine-grained synthetic peridotite under wet conditions. J. Geophys. Res. 105(B6):13535–53

Mecking H, Kocks UF. 1981. Kinetics of flow and strain-hardening. Acta Metallurgica. 29(11):1865–75

Mei S, Kohlstedt DL. 2000. Influence of water on plastic deformation of olivine aggregates: 2. Dislocation creep regime. J. Geophys. Res. 105(B9):21471–81

Mercier, Nicolas. 1975. Textures and Fabrics of Upper-Mantle Peridotites as Illustrated by Xenoliths from Basalts. J. Petrol. 16(2):454–87

Meyer GG, Brantut N, Mitchell TM, Meredith PG. 2019. Fault reactivation and strain partitioning across the brittle-ductile transition. Geology. 47(12):1127–30

Miyazaki T, Sueyoshi K, Hiraga T. 2013. Olivine crystals align during diffusion creep of Earth's upper mantle. Nature. 502(7471):321–26

Nabarro FRN. 1967. Steady-state diffusional creep. The Philosophical Magazine: A Journal of Theoretical Experimental and Applied Physics. 16(140):231–37

Ohuchi T, Kawazoe T, Higo Y, Funakoshi K i., Suzuki A, et al. 2015. Dislocation-accommodated grain boundary sliding as the major deformation mechanism of olivine in the Earth's upper mantle. Science Advances. 1(9):e1500360–e1500360

Parsons B, Richter FM. 1980. A relation between the driving force and geoid anomaly associated with mid-ocean ridges. Earth Planet. Sci. Lett. 51(2):445–50

Paterson MS. 1970. A high-pressure, high-temperature apparatus for rock deformation. International Journal of Rock Mechanics and Mining Sciences & Geomechanics Abstracts. 7(5):517–26

866 Peslier AH. 2010. A review of water contents of nominally anhydrous natural minerals in the mantles of
867 Earth, Mars and the Moon. J. Volcanol. Geotherm. Res. 197(1-4):239–58

868 Piazolo S, Bons PD, Griera A, Llorens M-G, Gomez-Rivas E, et al. 2019. A review of numerical
869 modelling of the dynamics of microstructural development in rocks and ice: Past, present and future.
870 J. Struct. Geol. 125:111–23

871 Pickering FB. 1976. The Basis of Quantitative Metallography. Metals and Metallurgy Trust for the
872 Institute of Metallurgical Technicians

873 Platt JP, Behr WM. 2011. Grainsize evolution in ductile shear zones: Implications for strain localization
874 and the strength of the lithosphere. J. Struct. Geol. 33(4):537–50

875 Precigout J, Prigent C, Palasse L, Pochon A. 2017. Water pumping in mantle shear zones. Nat. Commun.
876 8:15736

877 Prigent C, Warren JM, Kohli AH, Teyssier CP. 2020. Fracture-mediated deep seawater flow and mantle
878 hydration on oceanic transform faults. Earth Planet. Sci. Lett. 532:115988

879 Raj R, Ashby MF. 1971. On Grain Boundary Sliding and Diffusional Creep. Metallurgical Transactions.
880 2:1113–27

881 Richards F, Hoggard M, Crosby A, Ghelichkhan S, White N. 2020. Structure and dynamics of the oceanic
882 lithosphere-asthenosphere system. Phys. Earth Planet. Inter. 309:106559

883 Ricoult DL, Kohlstedt DL. 1985. Creep of Fe2SiO4 and Co2SiO4 single crystals in controlled
884 thermodynamic environments. Philos. Mag. A. 51(1):79–93

885 Royden LH. 1993. The tectonic expression slab pull at continental convergent boundaries. Tectonics.
886 12(2):303–25

887 Rudge JF. 2018. The Viscosities of Partially Molten Materials Undergoing Diffusion Creep. J. Geophys.
888 Res. [Solid Earth]. 123(12):10,534–10,562

889 Silber RE, Girard J, Karato S-I. 2022. Effects of pressure on diffusion creep in wet olivine aggregates.
890 Phys. Earth Planet. Inter. 324:106840

891 Skemer P, Hansen LN. 2016. Inferring upper-mantle flow from seismic anisotropy: An experimental
892 perspective. Tectonophysics. 668:1–14

893 Speciale PA, Behr WM, Hirth G, Tokle L. 2020. Rates of Olivine grain growth during dynamic
894 recrystallization and postdeformation annealing. J. Geophys. Res. 125(11):e2020JB020415

895 Sundberg M, Cooper RF. 2008. Crystallographic preferred orientation produced by diffusional creep of
896 harzburgite: Effects of chemical interactions among phases during plastic flow. J. Geophys. Res.
897 113:B12208

898 Takei Y, Holtzman BK. 2009. Viscous constitutive relations of solid-liquid composites in terms of grain
899 boundary contiguity: 1. Grain boundary diffusion control model. J. Geophys. Res. 114(B6):B06205

900 Tasaka M, Hiraga T. 2013. Influence of mineral fraction on the rheological properties of forsterite +
901 enstatite during grain-size-sensitive creep: 1. Grain size and grain growth laws. J. Geophys. Res.
902 118(8):3970–90

903 Tasaka M, Hiraga T, Zimmerman ME. 2013. Influence of mineral fraction on the rheological properties
904 of forsterite + enstatite during grain-size-sensitive creep: 2. Deformation experiments. J. Geophys.
905 Res. 118(8):3991–4012

906 Tasaka M, Zimmerman ME, Kohlstedt DL. 2015. Creep behavior of Fe-bearing olivine under hydrous
907 conditions. J. Geophys. Res. 120:6039–57

908 Tasaka M, Zimmerman ME, Kohlstedt DL. 2017. Rheological weakening of olivine plus orthopyroxene

aggregates due to phase mixing: 1. Mechanical behavior. J. Geophys. Res. 122(10):7584–96

Tasaka M, Zimmerman ME, Kohlstedt DL. 2020. Rheological Weakening of Olivine + Orthopyroxene Aggregates Due to Phase Mixing: Effects of Orthopyroxene Volume Fraction. J. Geophys. Res. [Solid Earth]. 125(9):e2020JB019888

Thom CA, Hansen LN, Breithaupt T, Goldsby DL, Kumamoto KM. 2022. Backstresses in geologic materials quantified by nanoindentation load-drop experiments. Philos. Mag. 102(19):1974–88

Toriumi M, Karato S-I. 1978. Experimental studies on the recovery process of deformed olivines and the mechanical state of the upper mantle. Tectonophysics. 49(1):79–95

Underwood EE. 1970. Quantitative Stereology. Reading, MA: Addison-Wesley Publishing Co.

Van der Wal D, Chopra P, Drury MR, Fitzgerald JD. 1993. Relationships between dynamically recrystallized grain size and deformation conditions in experimentally deformed olivine rocks. Geophys. Res. Lett. 20:1479–82

Vauchez A, Tommasi A, Mainprice D. 2012. Faults (shear zones) in the Earth's mantle. Tectonophysics. 558-559:1–27

Wallis D, Hansen LN, Kumamoto KM, Thom CA, Plumper O, et al. 2020. Dislocation interactions during low-temperature plasticity of olivine and their impact on the evolution of lithospheric strength. Earth Planet. Sci. Lett. 543:116349

Wang Z, Zhao Y, Kohlstedt DL. 2010. Dislocation creep accommodated by grain boundary sliding in dunite. J. Earth Sci. 21(5):541–54

Warren JM, Hirth G. 2006. Grain size sensitive deformation mechanisms in naturally deformed peridotites. Earth Planet. Sci. Lett. 248(1-2):438–50

930 Warren JM, Hirth G, Kelemen PB. 2008. Evolution of olivine lattice preferred orientation during simple
931 shear in the mantle. Earth Planet. Sci. Lett. 272(3-4):501–12

932 Watts AB, Zhong SJ, Hunter J. 2013. The Behavior of the Lithosphere on Seismic to Geologic
933 Timescales. Annu. Rev. Earth Planet. Sci. 41:443–68

934 Weertman J, Weertman JR. 1975. High Temperature Creep of Rock and Mantle Viscosity. Annu. Rev.
935 Earth Planet. Sci. 3(1):293–315

936 Whitehouse PL. 2018. Glacial isostatic adjustment modelling: historical perspectives, recent advances,
937 and future directions. Earth Surface Dynamics. 6(2):401–29

938 Wiesman HS, Zimmerman ME, Kohlstedt DL. 2018. Laboratory investigation of mechanisms for phase
939 mixing in olivine + ferropericlase aggregates. Philos. Trans. A Math. Phys. Eng. Sci.
940 376(2132):20170417

941 Wood BJ, Virgo D. 1989. Upper mantle oxidation state: Ferric iron contents of lherzolite spinels by 57Fe
942 Mössbauer spectroscopy and resultant oxygen fugacities. Geochim. Cosmochim. Acta. 53(6):1277–
943 91

944 Yabe K, Sueyoshi K, Hiraga T. 2020. Grain-Boundary Diffusion Creep of Olivine: 1. Experiments at 1
945 atm. J. Geophys. Res. [Solid Earth]. 125(8):e2020JB019415

946 Zhao N, Hirth G, Cooper RF, Kruckenberg SC, Cukjati J. 2019. Low viscosity of mantle rocks linked to
947 phase boundary sliding. Earth Planet. Sci. Lett. 517:83–94

948 Zhao Y-H, Ginsberg SB, Kohlstedt DL. 2004. Solubility of hydrogen in olivine: dependence on
949 temperature and iron content. Contrib. Mineral. Petrol. 147(2):155–61

950 Zhao Y-H, Zimmerman ME, Kohlstedt DL. 2009. Effect of iron content on the creep behavior of olivine:
951 1. Anhydrous conditions. Earth Planet. Sci. Lett. 287(1):229–40

952 Zhao Y-H, Zimmerman ME, Kohlstedt DL. 2018. Effect of iron content on the creep behavior of Olivine:
953 2. Hydrous conditions. Phys. Earth Planet. Inter. 278:26–33

954 Zhong S, Watts AB. 2013. Lithospheric deformation induced by loading of the Hawaiian Islands and its
955 implications for mantle rheology. J. Geophys. Res. 118(11):2013JB010408

956 Zimmerman ME, Kohlstedt DL. 2004. Rheological Properties of Partially Molten Lherzolite. J. Petrol.
957 45(2):275–98

958

8. Terms and Definitions

1. **Lithosphere:** outermost region of the solid earth, consisting of crust plus mantle portion that is effectively rigid on ~100 Myr timescale.
2. **Ductile deformation:** inelastic deformation without failure, which is sometimes referred to as flow.
3. **Low-temperature plasticity:** regime in which glide of dislocations, dislocation interactions, and strain hardening set the overall strain rate.
4. **Dislocation creep:** regime in which dislocation climb and associated diffusion lead to recovery, which moderates the glide rate and therefore strain rate.
5. **Dislocation-accommodated grain boundary sliding (GBS):** deformation within grains by dislocation motion associated with stress concentrations at the contacts between grains as a result of sliding (Langdon 2006).
6. **Diffusion creep:** stress concentrations associated with grain-boundary sliding are relieved by the mass diffusion of material (Coble 1963).
7. **Crystal-plasticity:** used in this review to refer to strain from the motion of dislocations.
8. **Brittle deformation:** permanent deformation through the creation and growth of cracks.
9. **Friction:** pressure-dependent deformation that can be stable or unstable. Included here under brittle deformation though it may not involve grain-scale cracking.
10. **Dislocation:** Linear defect in the crystal structure. Dislocations introduce slip into an otherwise perfect lattice, generating plastic strain of the crystal.
11. **Dislocation recovery:** Removal of dislocations by mutual annihilation of opposing dislocations or by incorporation into subgrain or grain boundaries.

12. **Strain hardening:** Strengthening of a material during ductile deformation due to the build-up of dislocations.

13. **Backstress:** the resistance to dislocation motion due to long-range elastic interactions among dislocations (also referred to as internal stress).

14. **Elastic thickness:** thickness of the region within the lithosphere that can elastically support stresses due to flexure without yield.

15. **Integrated strength of the lithosphere:** maximum stress that can be supported by the lithosphere integrated over depth, with units of force per length.

9. Sidebars

9.1. Pre-Exponential Factor (A_i)

The pre-exponential factor (A_i) is a scaling factor that combines material-dependent scaling factors for each component of the flow law (e.g., stress can be scaled by the shear modulus). The units of A_i vary as a function of the exponent values for each mechanism. For example, the units of A_i for dry, melt-free dislocation creep are $MPa^{-3.5}\ s^{-1}$ and for diffusion creep are $MPa^{-1}\ \mu m^3\ s^{-1}$. Modifying any term in Equation 1 (for example, n or C_{OH}) requires a corresponding modification to the pre-exponential factor. In addition, some parameters, particularly E_i*, exhibit strong covariance with A_i when calculated from experimental datasets, and therefore any modification of flow-law

parameters for testing purposes requires a corresponding modification of A_i to ensure that the modified flow law is still consistent with experimental data.

9.2. Water Fugacity (f_{H2O}) and Concentration (C_{OH})

The wet flow laws were originally determined by controlling water fugacity (f_{H2O}) during experiments, which is the formulation provided in Hirth & Kohlstedt (2003). Flow law parameters (A_{wet}, E^*_{wet}, V^*_{wet}) can be converted to concentration (C_{OH}) using the calibration of C_{OH} in terms of f_{H2O} from Kohlstedt et al. (1996) and updated by Zhao et al. (2004). We report this formulation in Equation 1.

In Table 1, we present the wet flow-law parameters based on C_{OH}, not f_{H2O}, as hydrogen abundances in natural samples are measured as concentrations. Two versions of the parameters are provided for the two units used to describe hydrogen in nominally anhydrous minerals: (1) C_{OH} in units of ppm H/Si, typically used for rock-deformation experiments, and (2) C_{OH} in ppm H_2O, typically used in geochemical studies. Units of ppm H/Si correspond to the weight fraction of hydrogen per 10^6 Si in the olivine lattice and thus reflect structural accommodation of hydrogen. The conversion factor between H_2O and H/Si is calculated from the molar weight and cation proportions of Si and H in the mineral and water. As mantle minerals typically have Mg/(Mg+Fe) = 0.90, the conversion factor by which ppm H_2O is multiplied to derive ppm H/Si is 16.3 for olivine (where 16.3 = [147 g/mol ÷ 1 Si cation]÷[18 g/mol ÷ 2 H cations]), 11.5 for orthopyroxene, and 12.2 for clinopyroxene.

9.3. Activation Volume (V)*

Most parameters in the olivine flow laws are constrained using a gas-medium Paterson apparatus (Paterson 1970), which has excellent resolution in stress, strain rate, and temperature but is limited to relatively low pressures (<400 MPa). Deformation-DIA experiments capable of achieving high pressures (≤9 GPa) have provided improved estimates of V^* for dry dislocation creep (Dixon & Durham 2018) and wet diffusion creep (Silber et al. 2022). Measurement of V^* for dry diffusion creep remains a challenge, as fine-grained samples adsorb water during the experiments (Silber et al. 2022). However, for most lithospheric depths, these constraints are adequate as pressure has a limited effect.

9.4. Chemical Environment

The rate of steady-state creep depends on the chemical environment, in addition to physical parameters such as stress and grain size. These effects are usually included implicitly in Equation 1 as limited data are available to provide explicit constraints. The viscosity of olivine decreases with increasing iron content (Ricoult & Kohlstedt 1985) and flow laws have been parameterized as a function of fayalite/forsterite content (Tasaka et al. 2015, Zhao et al. 2009, 2018). Silica activity also influences deformation, with weakening observed for orthopyroxene-buffered olivine relative to magnesiowustite-buffered olivine in single-crystal experiments (Bai et al. 1991).

The effect of oxygen fugacity (f_{O2}) can be explicitly included in Equation 1 as:

$$\dot{\varepsilon}_i = A_i \frac{\sigma^{n_i}}{d^{p_i}} f_{\mathrm{O}_2}^{m_i} c_{\mathrm{OH}}^{r_i} \exp\left(\alpha_i \phi\right) \exp\left(\frac{-\left(E_i^* + PV_i^*\right)}{\mathrm{R}T}\right),$$

where m is the oxygen fugacity exponent. The influence of f_{O2} on deformation of polycrystalline olivine has thus far only been measured in dislocation-creep experiments (Keefner et al. 2011):

m_{disc} = 0.20 ± 0.01, A_{disc} = $10^{2.6\pm0.3}$ s^{-1} $MPa^{-3.6}$ $Pa^{-0.2}$, and E^*_{disc} = 449 ± 7 kJ/mol. Their results indicate that viscosity decreases as conditions become more reducing and that this reduction occurs at conditions relevant to the lithospheric mantle, which is heterogeneous with respect to f_{O2} (e.g., Cottrell et al. 2022). However, f_{O2} is often overlooked in application of olivine flow laws because (1) controlling f_{O2} in deformation experiments is difficult, (2) constraints do not exist for all mechanisms, and (3) f_{O2} in natural peridotites can only be estimated if all phases (olivine, orthopyroxene, and spinel) involved in the spinel oxybarometer equilibria (Wood & Virgo 1989) are present.

9.5. Grain-Size Analysis

Grain size is measured on 2D images, typically using either linear-intercept or equivalent-area–diameter analysis (e.g., Underwood 1970). These measurements require a conversion factor to estimate the mean grain diameter in 3D, as most grains are measured in off-center sections in 2D images. Studies based on the linear-intercept technique typically apply a conversion factor of 1.5 to the mean grain size (Underwood 1970), but some studies use a correction of 1.75, following the method of Pickering (1976). Studies based on equivalent-area diameter use a scaling factor of $4/\pi$ (Underwood 1970). Tasaka et al. (2017) concluded that grain sizes determined by line-intercept are a factor of 1.07 larger than equivalent-area, while Speciale et al. (2020) concluded that the two methods are within error of each other. Most studies use the arithmetic mean to derive grain size, but the geometric mean provides a more representative estimate as grain-size distributions are approximately log-normal (Underwood 1970). Arithmetic mean estimates of grain size are a factor of 1.35 larger than geometric mean estimates (Warren et al. 2008). An important step in comparing

flow-law predictions to real rocks is to ensure that the same grain-size measurement technique is used as that used in calibrating the flow law.

9.6. Relationship Between Stress and Grain Size

For viscously deforming rocks, stress is typically estimated using a piezometer, which relates grain size to the macroscopic differential stress, assuming that recrystallization was driven by the movement of dislocations. For mantle rocks, the most commonly applied piezometers (Karato et al. 1980, Van der Wal et al. 1993) are calibrated by lab experiments on olivine-only aggregates. Alternatively, the wattmeter model treats grain size as a competition between grain growth and dynamic recrystallization (Austin & Evans 2007). Neither method accounts for the effects of secondary phases on migrating grain boundaries. The subgrain size piezometer of Goddard et al. (2020) provides a solution as subgrain size is unaffected by the presence of other phases. If grain size is modified by annealing due to growth following deformation (e.g., Boneh et al. 2017, Speciale et al 2020), then estimated stresses will be artificially lower, though the rate of grow is reduced in the presence of secondary phases (Tasaka & Hiraga 2013).

10. Captions, Tables & Figures

10.1. Figure Captions

Figure 1**:** (a) Schematic diagram of the lithosphere. White lines represent profile locations in (b) and (c). (b) Geotherms for 80 Myr oceanic lithosphere using a half-space cooling model and for a fast-slipping transform fault using a version of the model from Behn et al. (2007) updated by M. Boettcher (personal written communication). Both models assume a mantle potential temperature of 1300°C. (c) Strength-depth diagrams highlighting ductile behavior. The brittle-ductile transition occurs at shallow depth in the shear zone (calculated at a post-seismic strain rate of 10^{-8} s^{-1} and grain size of 1 μm) due to the operation of diffusion creep. The mature oceanic lithosphere exhibits a deeper transition from brittle processes to low-T plasticity and GBS. (d) Porphyroclastic peridotite representative of the lithospheric mantle (Tonga trench sample BMRG08-98-2-1). (e) Peridotite ultramylonite demonstrating the grain-size reduction and foliated texture associated with localized deformation (Shaka transform fault sample AII107-6-61-83). Photomicrographs taken in cross-polarized light.

Figure 2: Conceptual diagram illustrating the subgrain- and grain-scale processes that contribute to ductile deformation in olivine. The rate of each process depends on external conditions (temperature, pressure, stress, chemical environment). While all processes are always active, the extent to which an individual process accommodates deformation varies depending on conditions.

Figure 3**:** Strain rate as a function of stress at a range of grain sizes, *d*, and temperatures, *T*. Thick black curves indicate steady-state flow laws from Table 1, including diffusion creep from Hirth and Kohlstedt (2003), HK03, and the modified version from Hansen et al. (2011), HZK11. The

thin black line indicates the low-temperature plasticity flow law at yield. These curves are compared to the diffusion creep flow law from Yabe et al. (2020) and the dislocation creep flow laws from Breithaupt et al. (2020) and Gouriet et al. (2019).

Figure 4**:** Comparison of deformation data for olivine aggregates to different flow law formulations as a function of grain size. In each panel, all data are normalized to 200 MPa and 1200°C using the flow laws of interest in that panel. The recommended combination of flow laws from Table 1 are presented in (a) and (c).

Figure 5**:** Deformation mechanism maps at 80-km depth and dry conditions, corresponding to mature oceanic lithosphere. (a) Stress versus grain size at fixed temperature (800°C) and (b) stress versus temperature at fixed grain size (1 mm). Strain rate contours of 10^{-12}–10^{-15} s^{-1} (tectonic rates) are highlighted on each plot for comparison. These calculations use the dry flow laws in Table 1, including the HZK11 parameters for diffusion creep, which is the preferred option for use in combination with the GBS flow law.

Figure 6**:** Deformation mechanism maps for shear zones, calculated at conditions (800°C, ~10 km depth) relevant to oceanic transform faults. The HK03 parameters for diffusion creep of olivine (Table 1) are used in both maps, as these have the closest correspondence to multiphase lab experiments. (a) Deformation outside of the shear zone is set by the coarse-grained protolith, which consists of dry olivine with a grain size of ~1–10 mm. (b) Deformation within the shear zone is set by the mylonite, which has a grain size of ~1–10 μm and is water saturated. Material inside and outside of the shear zone feels the same stress, but material outside has not reached equilibrium grain size and deforms at a slower strain rate. Background tectonic strain rates of 10^{-12} and 10^{-15} s^{-1} are highlighted to aid comparison.

Figure 7**:** Examples of microstructures associated with the major olivine deformation mechanisms. Each dataset is an electron backscatter diffraction map plotted as the misorientation of each pixel relative to the mean orientation of the grain, which highlights deformation within grains due to dislocations. All panels use the same color-scale range of 0–20° misorientation, except for panel (a), which is plotted on a scale of 0–5° misorientation. Grains are defined by a minimum misorientation of 10° and grain boundaries are plotted as black lines. These maps are overlaid on a gray-scale band contrast map, with darker gray indicating lower quality diffraction patterns. Gray pixels indicate (i) areas that could not be indexed for orientation due to cracks and alteration phases and are thus dark gray to black and (ii) areas with secondary minerals such as pyroxene for which orientation data are not shown.

(a) Low-temperature plasticity in experiment San382 on a San Carlos olivine single crystal (adapted from Wallis et al. 2020 (CC BY)).

(b) Low-temperature plasticity in lherzolite sample Ba1g from the Balmuccia orogenic peridotite, Italy (adapted from Matysiak & Trepmann 2012, with permission from Elsevier).

(c) Dislocation creep in dunite experiment PI-1191 (adapted from Keefner et al. 2011 (CC BY), with permission from Wiley).

(d) Dislocation creep in garnet harzburgite xenolith H02-9E from the Homestead kimberlite, Montana (adapted from Chin et al. 2021, with permission from Elsevier).

(e) GBS in dunite experiment PI-1543 (adapted from Hansen et al. 2011, copyright 2011 by the American Geophysical Union). [**Note to Annual Reviews: I am an author of this

article; the publisher grants authors the right to reuse their own figures without permission.**]

(f) GBS in dunite sample 3923J13 from the Josephine Peridotite (adapted from Hansen & Warren 2015 (CC BY-NC-ND), with permission from Wiley).

(g) Diffusion creep in dunite experiment PI-81 from Hirth and Kohlstedt (1995a) and mapped by Zhao et al. (2019).

(h) Diffusion creep in abyssal peridotite AII107-6-61-80 from the Shaka oceanic transform fault.

Figure 8**:** Comparison of predictions from laboratory experiments to geophysical observations. (a) Strength-depth diagram for oceanic lithosphere from olivine flow laws (Table 1), the onset of microcracking for intact rock (Baud et al. 2014), and friction on mature faults (Byerlee 1978). Also presented are theoretical models for crystal-plastic deformation of olivine (Breithaupt et al. 2020, Gouriet et al. 2019). The shaded gray field is the brittle-ductile transition, assuming the upper limit is set by the transition from brittle to crystal-plastic yield and the lower limit is set by the transition from frictional sliding to steady-state creep. (b) Depth evolution of lithosphere strength. Limits for the brittle-ductile transition are compared to geophysical estimates of elastic thickness based on flexure at trenches (squares, Hunter & Watts 2016) and at seamounts/islands (circles, Watts et al. 2013). (c) Comparison of predictions for integrated strength from (a) to estimates inferred from ridge push (Parsons & Richter 1980), slab pull (Royden 1993), gravitational potential energy in the Indian Ocean from neighboring continental lithosphere (Martinod & Molnar 1995), and strength profiles that best fit flexural data at trenches (Hunter & Watts 2016) and Hawaii (Bellas et al. 2020). These estimates are all weaker than the strength at steady-state predicted by experimental data.

1161 *10.2. Table 1*

1162 Table 1: Compilation of flow law parameters

Table 1: Flow law parameters

Parameter[a]	A	ρ	σ_b			E*	Σ
Units[b]	$m^2\ s^{-1}$	m^{-2}	10^6 Pa			(10^3 J/mol)	10^6 Pa
Olivine							
Low-T Plasticity (yield)	$10^{(-1.32)}$	$10^{(14.8)}$	0			450	3100
Low-T Plasticity (steady state)[c]	$10^{(-1.32)}$	$10^{(10)}$	1800			450	3100
Parameter	A	n	p	r	α	E*	V*
Units	$s^{-1} * (10^6\ Pa)^{-n} * (10^{-6}\ m)^p * COH^{-r}$	(stress)	(grain size)	(water)	(melt)	10^3 J/mol	$10^{-6}\ m^3$/mol
Olivine							
dry dislocation	1.1×10^5	3.5 ± 0.3	0	n.a.	30-45	530 ± 40	15 ± 5
wet dislocation (COH in units ppm H/Si)	20	3.5 ± 0.3	0	1.2	30-45	480 ± 40	11
wet dislocation (COH in units ppm H2O)	570	3.5 ± 0.3	0	1.2	30-45	480 ± 40	11
dry GBS	$10^{(4.8 \pm 0.8)}$	2.9 ± 0.3	0.7 ± 0.1	n.a.	30-45	445 ± 20	15 ± 5
dry diffusion (HK03)[d]	1.5×10^9	1	3	n.a.	30	375 ± 50	6 ± 4
dry diffusion (HZK11)[d]	$10^{(7.6)}$	1	3	n.a.	30	375 ± 50	6 ± 4
wet diffusion (C_{OH} in units ppm H/Si)	2.9×10^5	1	3	1	30	335 ± 75	1.9 ± 0.4
wet diffusion (C_{OH} in units ppm H_2O)	4.7×10^6	1	3	1	30	335 ± 75	1.9 ± 0.4
Orthopyroxene							
dry dislocation	$10^{(8.6 \pm 0.7)}$	3	0	n.a.	n.d.	600 ± 21	n.d.
Clinopyroxene							
dry dislocation	$10^{(9.8 \pm 0.5)}$	4.7 ± 0.2	0	n.a.	n.d.	760 ± 40	n.d.

Footnotes:

[a]Most parameters are from Hirth & Kohlstedt (2003), with the following exceptions:
Wet flow laws: Values fo A have been recalculated based on the updated water calibration (Bell et al., 2003) using a correction factor of 3.5 and Equation 5.
Dry diffusion (HZK11): The value for A_{diff} is from Hansen et al. (2011) and should be used in combination with the dry GBS flow law of Hansen et al. 2011.
Dry GBS: Values for A, n, p, and E* from Hansen et al. (2011). Value for V* assumed to be the same as for dry dislocation creep (Dixon & Durham, 2018).
Activation volume: Dry dislocation creep from Dixon & Durham (2018). Wet diffusion creep from Silber et al. (2022).
Opx dry dislocation: Parameters from Bystricky et al. (2016).
Cpx dry dislocation: Parameters from Bystricky & Mackwell (2001).
Abbreviations: n.a. = not applicable; n.d. = no data

[b]Units for Equation 1: strain rate in s^{-1}, stress in 10^6 Pa (i.e., MPa), grain size in 10^{-6} m (i.e., micron), C_{OH} in ppm H/Si or ppm H_2O, temperature in Kelvin, pressure in Pa, and R in in J/mol/K.

[c]Low-T plasticity (steady state): Only valid for $\sigma > \sigma_b$

1163 [d]Dry diffusion creep: See text for discussion of the two versions: HK03 = Hirth & Kohlstedt, 2003; HZK11 = Hansen et al., 2011.

1164

1165

1166

1167

10.3. Figure 1

Figure 1: Schematic diagram of the lithosphere

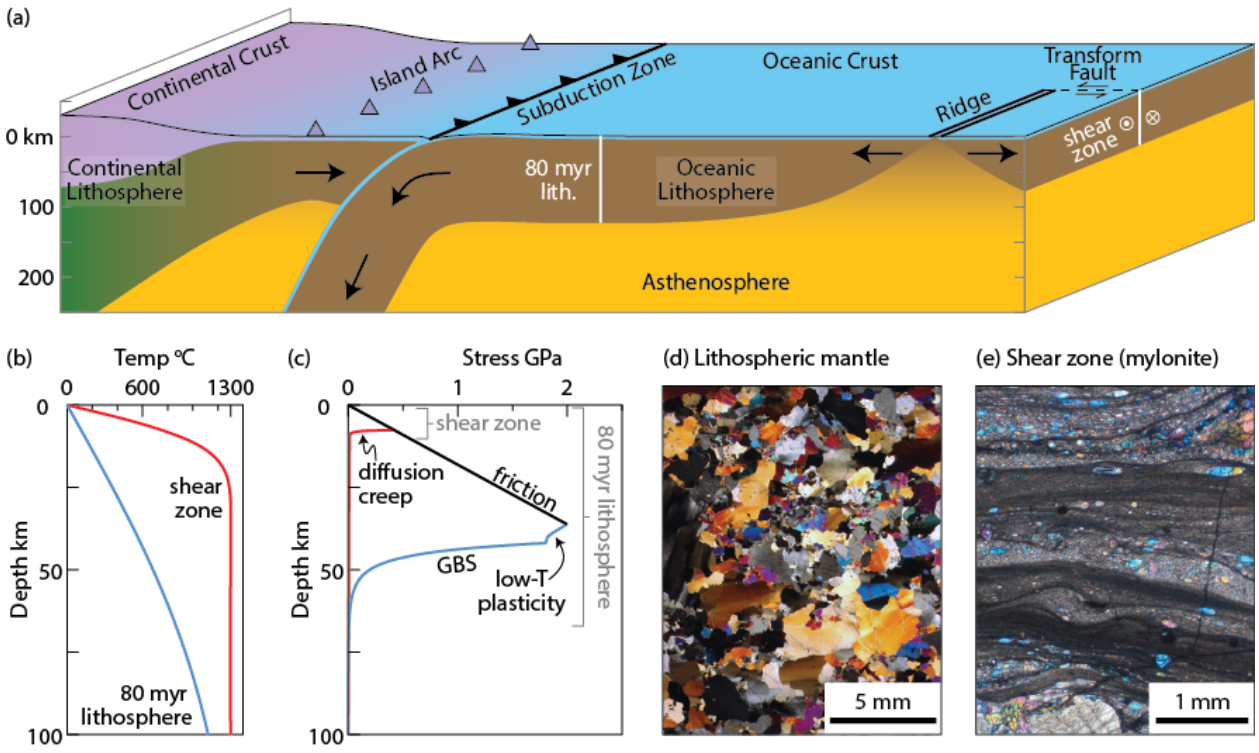

1176 *10.4.* Figure 2

1177 Figure 2: Schematic diagram of subgrain- and grain-scale processes accommodating ductile

1178 deformation.

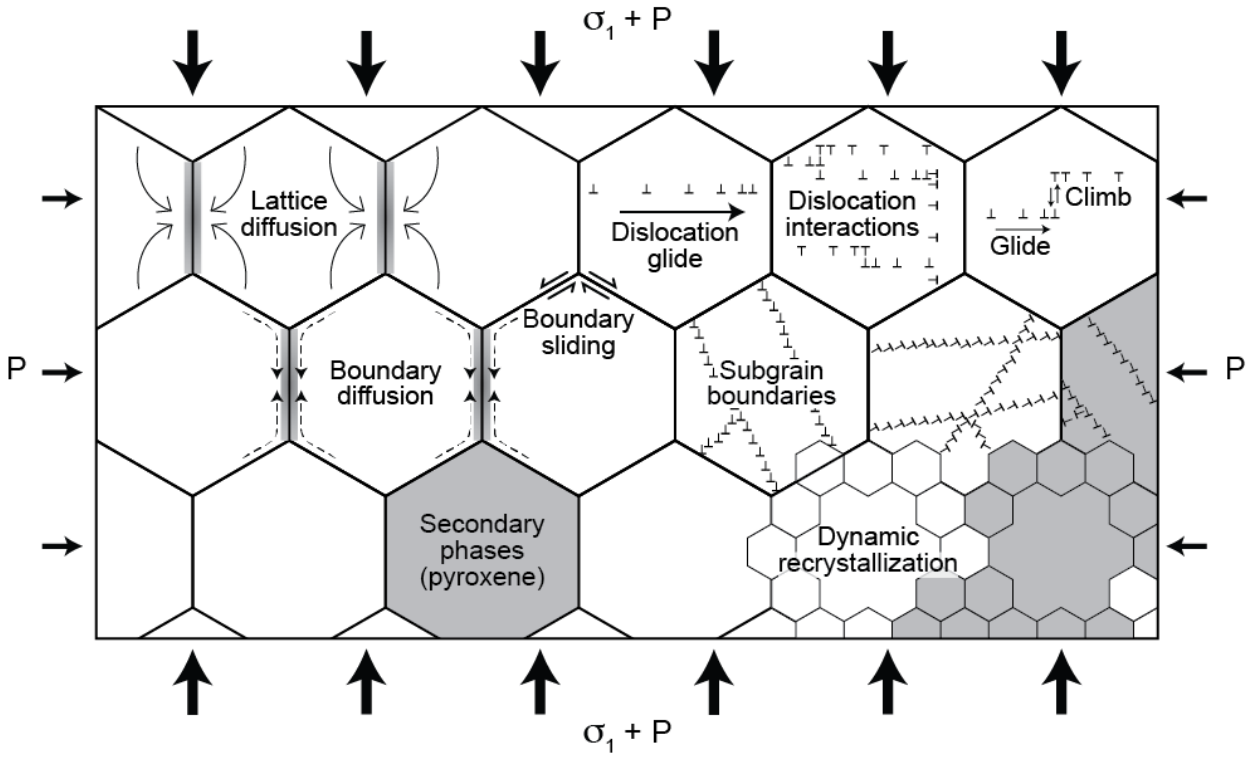

1179

1180

1181

10.5. Figure 3

Figure 3: Strain-rate vs stress comparison of laboratory-derived flow laws and models

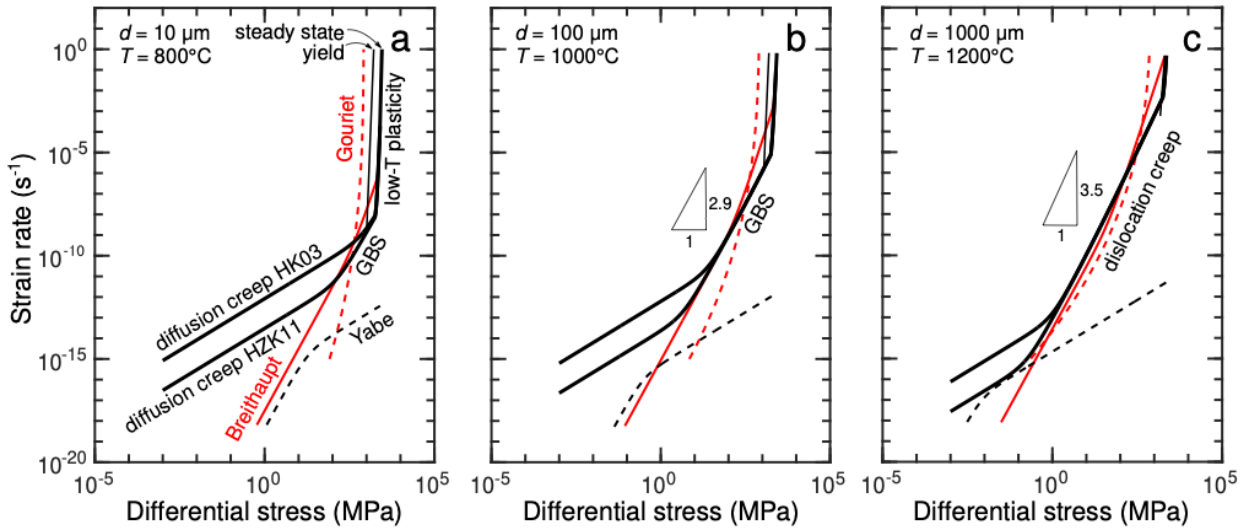

10.6. Figure 4

Figure 4: Strain rate vs grain size comparison of lab data to different flow law formulations

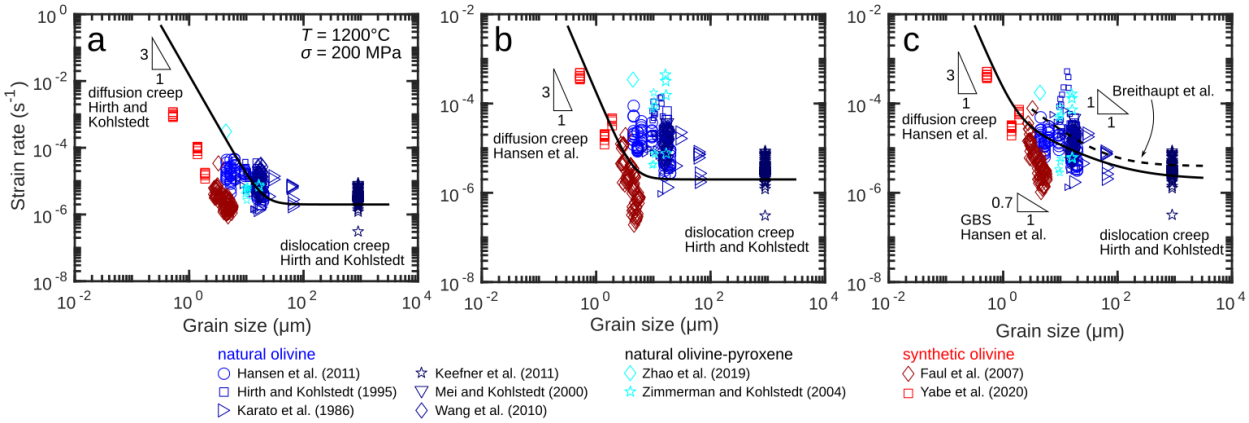

10.7. Figure 5

Figure 5: Deformation mechanism maps for mature oceanic lithosphere

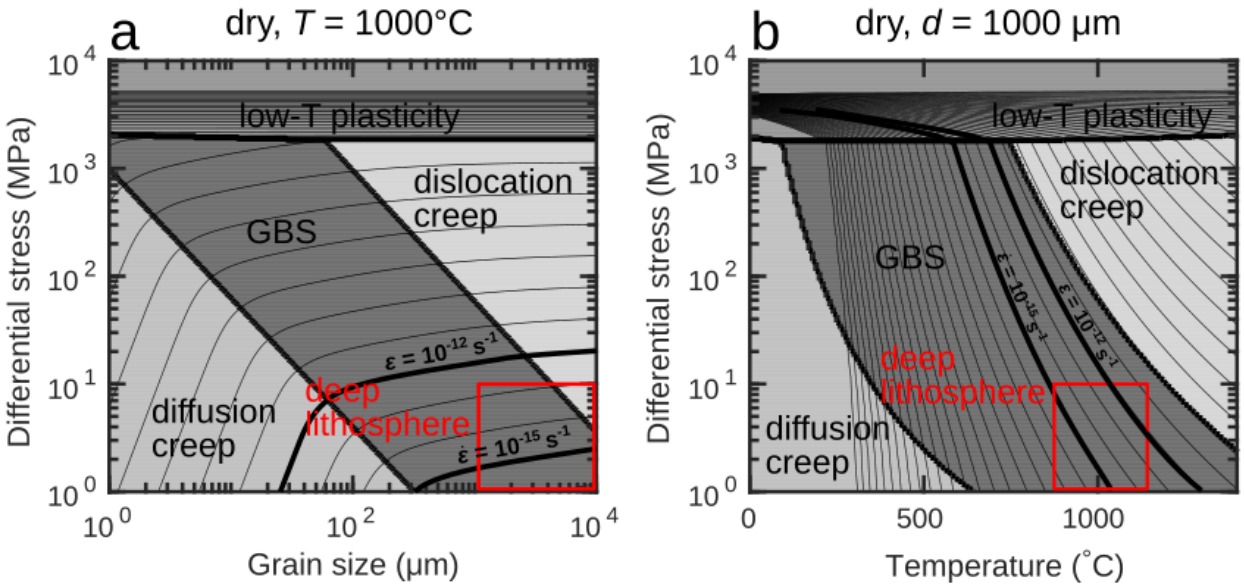

10.8. Figure 6

Figure 6: Deformation mechanism maps for shear zones

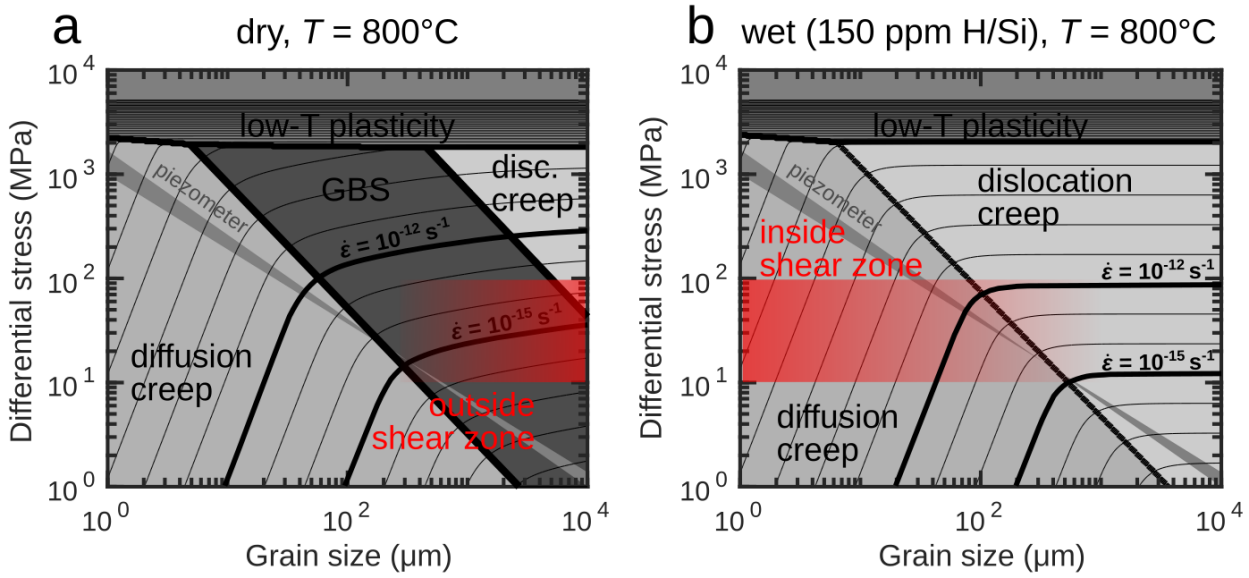

10.9. Figure 7

Figure 7: Olivine microstructures

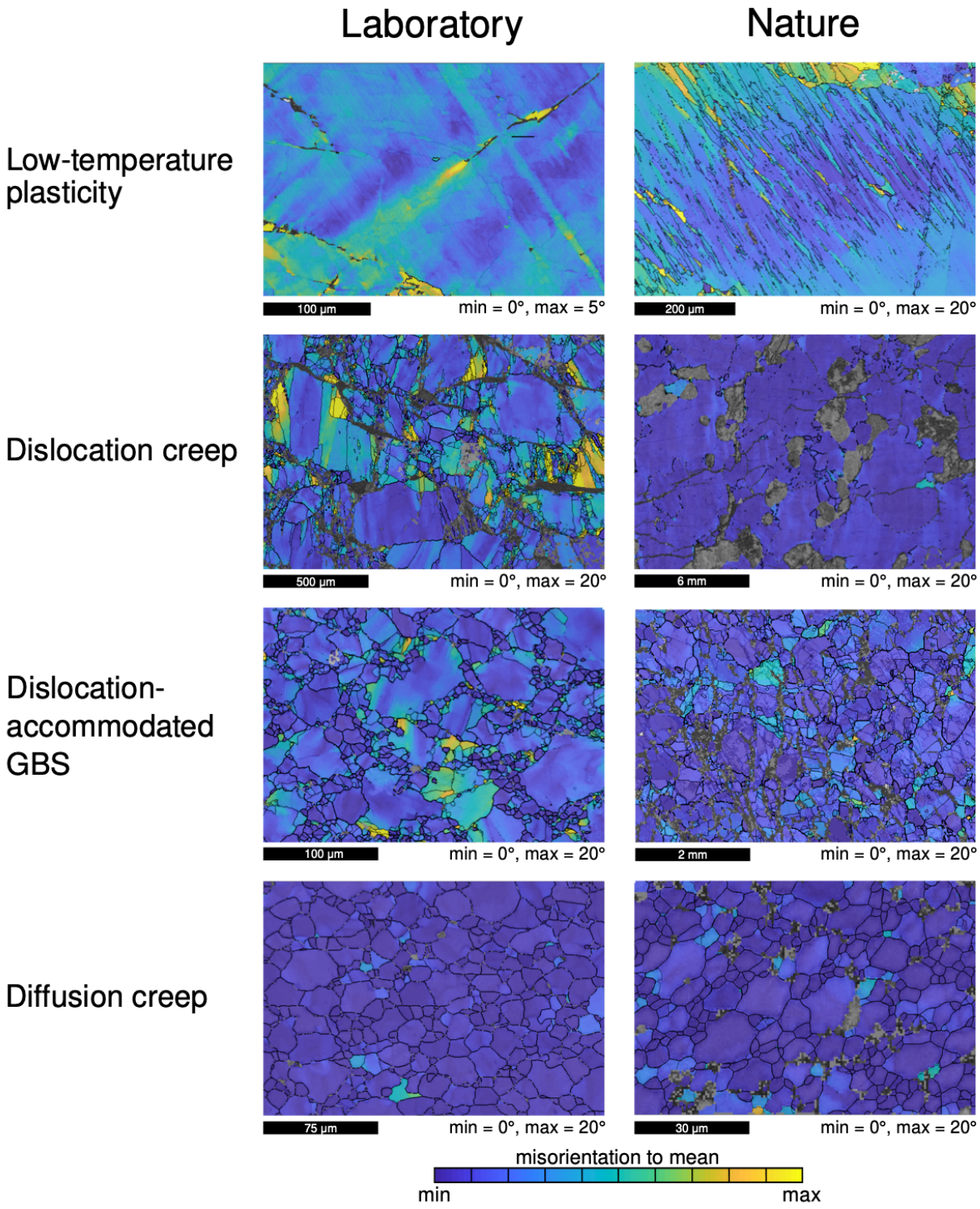

10.10. Figure 8

Figure 8: Comparison of flow laws to geophysical observations